Impact Load Mitigation of Meta-panels with Single Local Resonator

Nhi H. Vo[1], Thong M. Pham[2], Hong Hao[3], Kaiming Bi[4], and Wensu Chen[5]

Center for Infrastructural Monitoring and Protection, School of Civil and Mechanical Engineering, Curtin University, Kent Street, Bentley, WA 6102, Australia

Abstract

This study investigates the influence of design parameters on the impact mitigation capacity of a new meta-panel that leveraged the coupled mechanisms of plastic deformation and local resonance to absorb energy from impact loading. The main objective is to minimize the force to be transmitted to the protected structures through mitigating the stress wave propagation by using local resonators. The meta-panel demonstrates the capability of filtering out the stress wave induced by impact loading with frequencies falling in its bandgaps. A numerical model is built and verified by the analytical solution with a good agreement in terms of the predicted frequency bandgaps. The meta-panel shows a substantial reduction in the mid-span deflection of the facesheets and an increase in the impact energy absorption as compared with the conventional sandwich panels. The peak reaction force of the meta-panel transmitted to the protected structure is also reduced significantly by more than 47% compared to its conventional counterparts. Furthermore, parametric studies are conducted to investigate the effects of the thickness of the hollow-truss bar, core material properties, and impact velocity on the meta-panels impact-resistant behaviour.

[1] PhD Scholar. Email: hoangnhi.vo@postgrad.curtin.edu.au

[2] Senior Lecturer, Corresponding author. Email: thong.pham@curtin.edu.au

[3] John Curtin Distinguished Professor, Corresponding author. Email: hong.hao@curtin.edu.au

[4] Associate Professor. Email: Kaiming.bi@curtin.edu.au

[5] Associate Professor. Email: wensu.chen@curtin.edu.au

Keywords: Meta-structure; Meta-panel; Resonator; Sacrificial structures; Stress wave mitigation; Impact-resistance.

Nomenclature

A	Nominal cross-section of the soft layer (m^2)
E	Young's modulus of materials (GPa)
E_c	Young's modulus of soft layer (GPa)
G	Shear modulus of materials (kN/m)
k_1	Axial stiffness of the spring (kN/m)
k_2	Shear stiffness of the spring (kN/m)
k_{eff}	Dynamic effective stiffness (kN/m)
l	Length of the resonator (m)
L	Distance between two adjacent unit cells (m)
m_1	Mass of the resonator (kg)
m_{eff}	Dynamic effective mass (kg)
q	Wavenumber
r	Radius of the resonator (m)
t	Thickness of the outer tube (m)
T	Transmission coefficient
u	Displacement of resonator (m)
v	Velocity of the impactor (m/s)
ρ	Density of materials (kg/m^3)
ρ_c	Density of resonator (kg/m^3)
ϑ	Poisson's ratio of materials
ω	Angular frequency (rad/s)

1. Introduction

When structural elements, e.g., beams [1], [2], columns, and joints [3] are subjected to impulse loading, their failure/wreckages might cause major loss of human life and economy. It is, therefore, deemed important to develop protective systems to protect critical structures exposed to these threats. Amongst many mitigation strategies, the deployment of sacrificial cladding as a shock attenuator has attracted intensive researches due to its protective functionality and excellent behaviour [4], [5], [6], [7], [8]. Sacrificial claddings often consist of two components, namely the outer facesheets and the inner core [9], [10], [11]. While distributing the load more uniformly is the function of the outer facesheets, the inner core often deforms and absorbs most of the energy from the incident loading via plastic deformation, leading to load mitigation on the main protected structures. Many researches have proven that sandwich panels functioning as sacrificial claddings have a significantly higher dynamic resistance compared to the monolithic plates with the same mass per unit area [12].

Regarding the dynamic mitigation, much effort has been devoted to exploring different forms of protective sandwich panels as sacrificial cladding. Relatively new materials that possess the protective capabilities against dynamic loading have been explored by a few researchers such as aluminium foam panels by Hanssen et al. [13], double-layer foam panels by Ma and Ye [14], and honeycomb core by Hazizan and Cantwell [15], etc. Besides, the superior behaviour of the lattice-truss panels under impact loading has also been explored [16], [17], [18], [19]. These studies proved that the lattice core-based sandwich panels outperform their conventional counterparts such as honeycomb sandwich panels regarding impulsive energy absorption capacity and mitigating effect. Besides, the space provision of the lattice sandwich structures is generally wider compared to honeycomb structures, which can be utilized for other purposes, e.g. heat transfer [20], [21], energy absorbers [22], and sound isolation [23], [24]. Generally, the main mechanism of these types of sandwich panels is based on plastic deformation to absorb energy from the incident loading [25], [26], [6], [27], [28].

More recently, increasing attention has turned to filter incident loading using the local resonances as energy absorbers, e.g. meta-lattice truss bar [29], [30], [31], meta-concrete [32], [33], [34], [35], [36] and metamaterials [37] resulting in the loading mitigation effect. It is worth mentioning that the prefix "meta" originates from the Greek preposition, which meant "beyond", implying these exotic structural behaviour are superior to other natural counterparts [31]. To filter incident loading, Liu et al. [30] proposed the novel meta-truss bar comprising of single and dual resonators. Investigations have been carried out to manifest the exotic potential of the meta-truss bar in creating bandgaps to stop wave propagation. For practical applications, the wave propagation mitigation of the meta-structures has been demonstrated in meta-sandwich beam by Chen et al. [38]. The results showed that the local resonance of the embedded resonators in the meta-sandwich beam was activated when the frequencies of the incident loading fall into its bandgaps, thus trapping wave energy to attenuate stress wave propagation. Also, it has been proven that the bandgap is programmable by varying the resonator designs and thus allowing for tailoring the attenuation properties as required by practical applications [39]. A meta-foundation that can both attenuate seismic waves and withstand static loads was proposed by La Salandra et al. [40]. That study investigated the influence of both geometrical and mechanical properties of a foundation inspired by metamaterial concept on its dynamic performance as well as its capabilities of bearing gravity loads. Furthermore, the structural configuration of lattice core sandwich panels and the extraordinary characteristics of the meta-lattice truss bar to form a meta-panel, resulting in the impact/blast mitigation and higher energy absorption of the panels have been studied [31, 41]. In general, studies on applying meta-lattice truss bar in engineering structures are very limited and no systematic studies have been reported to determine the integral influence that affect the transient response of the meta-panel in literature. In particular, the effects of the design parameters including material properties and truss-bar thickness, as well as the impact velocity on the protective effectiveness of the meta-panel have not been well investigated. Given the above considerations, there is thus a strong need to further study of this promising field towards practical applications.

The impact behaviour of the meta-panel with single resonators functioning as sacrificial cladding (Fig. 1) are examined in this study. It should be noted that the meta-panel adopts the coupled mechanisms of absorbing strain energy through plastic deformation of the outer tube and local resonance of the inclusions. The optimization analyses are carried out to enhance its mitigating effect through comprehensive parametric studies. The impact performances of the meta-panel are simulated using finite element software LS-DYNA to evaluate its impact mitigation capacity compared to those of the conventional panels. The numerical transmission coefficient is verified against the analytical results for validation. In this study, the dynamic responses of panels with various designs are evaluated through the criteria including the energy absorption capacity, the central deflections of the facesheet, and the boundary reaction forces. Furthermore, parametric studies have been conducted by varying each parameter to investigate the effects of the truss-bar thickness, the material properties, and the impact velocity on the transient responses or the protective effect of the meta-panel. This study not only numerically and analytically demonstrates the dynamic mitigation mechanism of the meta-panel subjected to impact loads, but presents several favourable findings, which are beneficial for engineering applications. Experimental tests will be carried out in near future to further verify the performance of meta-panels designed according to these findings.

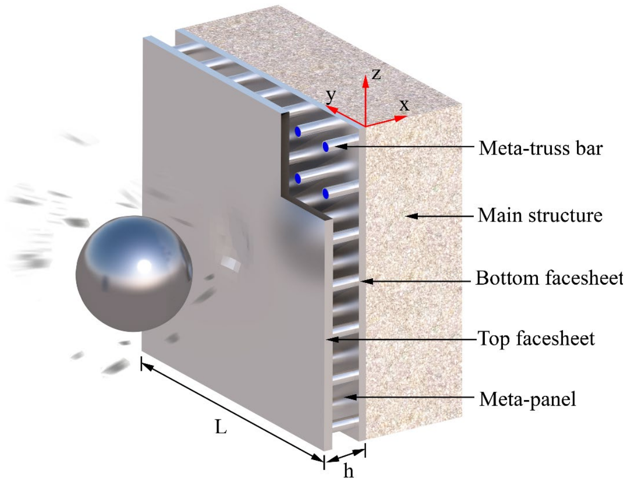

Fig. 1. Schematic illustration of the protection of meta-panels against impact loading.

2. Geometric configuration

For the investigated structure, two thin facesheets are bonded to four meta-truss bars to form a symmetric meta-panel as sketched in Fig. 2(a). The distinctive feature of this design lies in the meta-cores made of meta-lattice truss bars that consist of 7 unit cells (Fig. 2(b)). With this configuration, the unit model comprises three components, i.e. the hollow truss bar, the soft coat, and the resonator, whose dimensions are depicted in Figs. 2(b) while their materials are shown in Fig. 2(c). To endure large deformation, polyurethane (PU) is selected for the soft coating while aluminium 1060 and lead are respectively chosen for the truss bars and the resonator. The two facesheets connected rigidly to the outer tubes to form an integral structure are also made of aluminium 1060. The mechanical properties of all components are tabulated in Table 1.

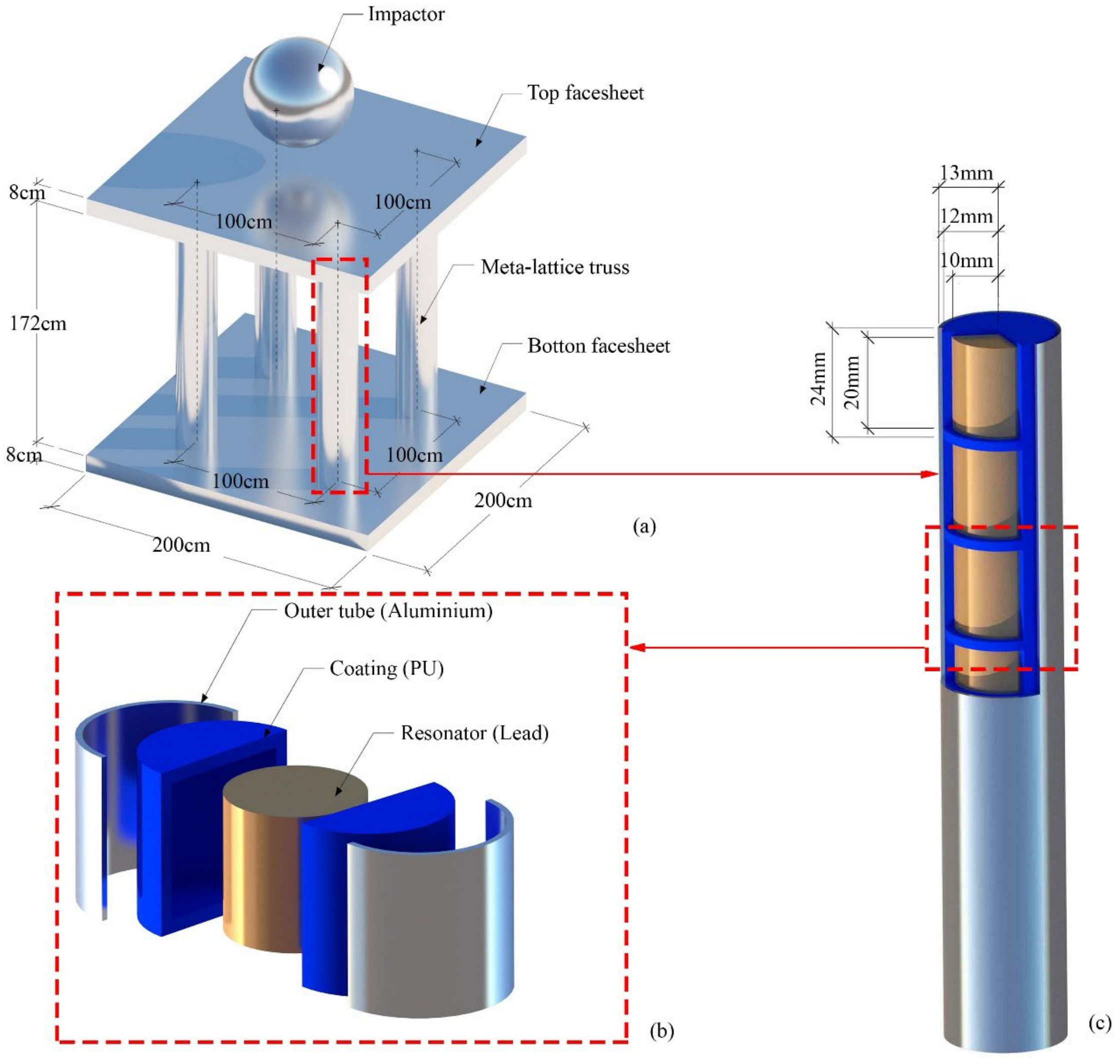

Fig. 2. Schematic diagrams of (a) the meta-panel under impact loads, (b) meta-truss bar, and (c) unit cell.

Table 1. Elastic material properties for all components

Materials	Density ρ (kg/m^3)	Young's modulus E (GPa)	Poisson's ratio v
Aluminium 1060	2,770	70	0.33
PU	900	0.147	0.42
Lead	11,400	16	0.44
Steel	7,850	210	0.29

3. Analytical predictions of the bandgaps

The design can be conceptualized as the monotonic unit cells as shown in Fig. 3, which are analytically described using the spring-mass model. The outer tube represents the matrix in the model while the resonator is represented by the mass of m_1. The soft coating is modelled by two springs including the axial spring and the shear spring, i.e., k_1, k_2, respectively for the soft coating. Without loss of generality, the mitigation effects on stress wave propagation of the meta-truss bar are examined by analyzing the performance of elastic stress wave propagation in the idealized meta-truss bar model.

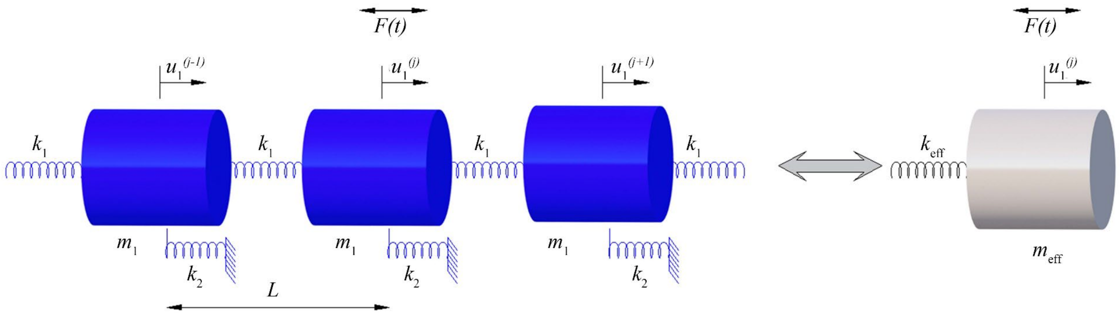

Fig. 3. Equivalent effective spring-mass model.

The mass of the resonator m_1 (with an outer radius, r) can be calculated as

$$m_1 = \rho \pi r^2 l \tag{1}$$

where ρ is the material density, r and l are the radius and length of the resonator.

The stiffness of the equivalent springs are estimated using the following equations:

$$k_1 = \frac{E_3 A_1}{l_1},\ k_2 = \frac{G_3 A_2}{l_2}, G_3 = \frac{E_3}{2(1+\vartheta_3)} \tag{2}$$

where G_3 and E_3 respectively denote shear and Young's modulus of the soft coating while ϑ_3 is Poisson's ratio. The determination of the nominal dimension for calculating the equivalent axial and shear spring stiffness, i.e, A_i and l_i (i=1,2), k_1 and k_2 are not straightforward due to the shape complex geometry. Instead of calculating these equivalent geometrical dimensions, in this study, the equivalent stiffness k_1 and k_2 are numerically calculated as presented in the appendix. It should be noted that the investigation on the relationships between the numerically determined stiffnesses with their theoretical values when varying the thickness l_1 and l_2 demonstrates that both numerical and analytical soltions yield similar estimations of stiffnesses for the considered meta-truss bar, as proven in previous studies [29, 31, 41, 42]. The estimated mass is given by m_1 = 7.16x10^{-2} kg while the axial and shear stiffness are k_1 = 57,375 kN/m, k_2 = 35,498 kN/m, respectively.

The characteristics of the meta-truss bar are determined by a process of deduction starting with applying the equation of motion and ending with the negative effective properties, as well as the dispersion relation and transmission coefficients. The equation of motion for the j^{th} unit cell can be derived as:

$$m_1 \frac{\partial^2 u_1^{(j)}}{\partial t^2} + k_1 \left(2u_1^{(j)} - u_1^{(j+1)} - u_1^{(j-1)}\right) + k_2 u_1^{(j)} = 0 \tag{3}$$

in which u_1 represents mass displacement.

The displacement for the harmonic wave of the j^{th} unit cell is expressed as:

$$u^{(j)} = Ue^{i(jqL-\omega t)} \tag{4}$$

where ω and L respectively denote the angular frequency and the distance between two adjacent unit cells. U and q stand for the wave amplitude and wave number, respectively.

Substituting Eq. (4) into Eq. (3), the dispersion curve is expressed:

$$cos(qL) = 1 + \frac{k_2 - m_1\omega^2}{2k_1} \tag{5}$$

To simplify the model, a homogeneous unit cell [30] consisting of an effective mass connected by an effective stiffness as shown in Fig. 3 can be derived and expressed as:

$$m_{eff} = m_1 - \frac{k_2}{\omega^2} \tag{6}$$

$$k_{eff} = k_1 - \frac{1}{4}\left(m_1 - \frac{k_2}{\omega^2}\right)\omega^2 \tag{7}$$

where m_{eff} and k_{eff} are the effective mass and effective stiffness, respectively. It is worth mentioning that the underlying goal for developing the effective properties of the investigated parameters including mass and stiffness in the analytical model is to establish the relationship between the frequency of the incident force and the locally resonant frequency of the system. In the local resonant phase, there is a relative and out-of-phase motion between the resonators and the truss tube. This induces a change in the vibration properties of the system, meaning that the effective parameters for the dynamic response are different from their physical parameters owing to the local vibrations. The negative effective mass and stiffness are triggered with incident frequencies falling into the bandgaps of the meta-truss bar, leading to the favourable wave attenuation characteristics of the meta-system.

The dispersion relation in Eq. (5) is solved to define the width of the passband as:

$$\omega = \sqrt{\frac{2k_1\left(1 - cos(qL)\right) + k_2}{m_1}} \tag{8}$$

The starting point of the passband can be obtained by substituting qL=0:

$$\omega = \sqrt{\frac{k_2}{m_1}} \tag{9}$$

and the ending point of the passband can be expressed by substituting qL=π, as:

$$\omega = \sqrt{\frac{4k_1 + k_2}{m_1}} \tag{10}$$

The transmission coefficients of the entire system can be given:

$$T = \left| \prod_{j=1}^{N} \frac{u^{(j)}}{u^{(j-1)}} \right| = \prod_{j=1}^{N} T^{(j)} \tag{11}$$

Based on the above derivations, Fig. 4(a) depicts the analytical dispersion relation of the meta-truss bar whereas the effective parameters are also obtained and shown in Fig. 4(b). It is observed that the theoretical first bandgap of the meta-truss bar is at [0 - 3,500] Hz, which is generated by the negative effective mass (as shown in Fig. 4(b)) while the value of effective stiffness becomes negative leading to the second bandgap at [> 9,500] Hz. It is shown that the bandgaps can be generated by both negative effective mass and stiffness.

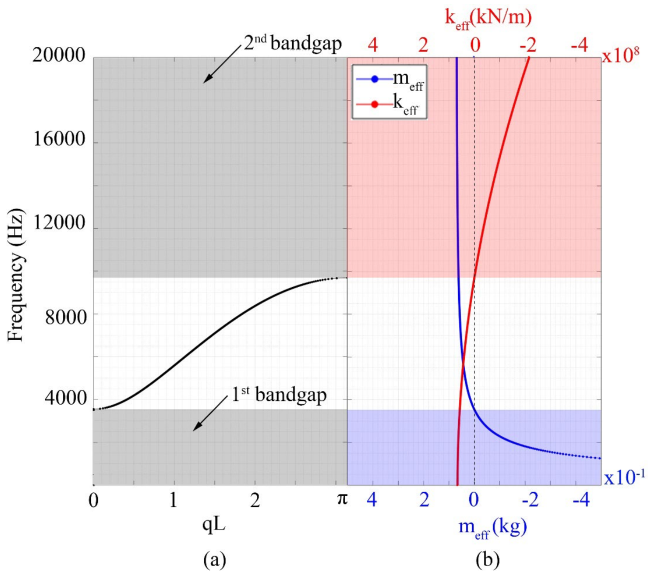

Fig. 4. (a) Dispersion curve and (b) effective parameters of the meta-truss bar.

4. Numerical modeling

The bandgap frequencies of the meta-truss bar have been achieved by utilizing the analytical solutions, based on the one-dimensional mass-in-mass model. However, the above theoretical derivation is based on the assumption of the infinite number of unit cells under harmonic wave input for solving the Eigen frequency and calculating the bandgaps. It is not straightforward to obtain the closed-form theoretical solutions of the case with a finite number of cells, boundary reflections, and subjected to different forms of input. Moreover, it is more difficult to derive the analytical solution of the structural behaviour of the meta-panel under impact load, especially when plastic deformation is considered. To surmount the limitations of the analytical solutions, a numerical investigation is conducted to evaluate the transient responses of the meta-panel subjected to impact loading. The results obtained from the above theoretical solutions based on idealized conditions are utilized to indirectly verify the accuracy of the numerical model of the meta-panel presented in Fig. 2 in Section 2.

4.1 Numerical model calibrations

The numerical simulation is conducted by the commercial software LS-DYNA [43] to evaluate the transient responses of the meta-panel subjected to impact loads. This section presents the constitutive material models, initial conditions, element types and sizes, and contact definition of the numerical model.

4.1.1 *Constitutive material models*

Johnson-Cook material model [44] as defined in Eq. 12 is adopted in LS-DYNA with the keyword *MAT_JOHNSON_COOK material (Mat_15) to exhibit the rate-dependence of aluminium material. The Johnson-Cook strength model, which is a phenomenological model based on various experimental results, has been widely used to capture the rate-dependent behaviour of aluminium alloy. The model has been successfully validated to describe the mechanical responses of Aluminium experiencing high-rate deformation or melting process [45].

$$\sigma_{eq} = \left[A + B\varepsilon_{eq}^{n}\right](1 + Cln\dot{\varepsilon}^{*})(1 - T^{*m}) \tag{12}$$

where the equivalent von Mises stress is denoted by σ_{eq} while the equivalent plastic strain is expressed by ε_{eq}. The plastic strain rate, $\dot{\varepsilon}^{*}$ is defined by the ratio $\dot{\varepsilon}/\dot{\varepsilon}_0$, in which $\dot{\varepsilon}_0$ is a reference strain rate and is generally set to 1.0 s^{-1}. The ratio $\frac{(T-T_r)}{(T_m-T_r)}$ defines the dimensionless temperature, T^*, in which the material reference temperature is T_r and the melting temperature is T_m. Besides, Table 3 gives the equation of state for the Johnson-cook model, which is adopted by card *EOS_LINEAR_POLYNOMINAL. The card *MAT_MOONEY_RIVLIN_RUBBER in Eq. (13) is simulated the performance of the PU material model while for the lead cores, the keyword *MAT_PLASTIC_KINEMATIC in Eq. (14) is chosen. It is because this material model is commonly used for modelling metal with bi-linear elastic-plastic constitutive relationship and isotropic or kinematic hardening plasticity which is defined by a hardening parameter β. In this study, β is set to 1 which represents isotropic hardening. The steel impact ball is assumed as rigid and modelled by the card *MAT_RIGID. The material properties used in the numerical simulation are listed in Table 2.

Soft materials have nonlinear stress-strain behaviour for relatively large deformations. Under such conditions, they are generally assumed as nearly incompressible. To model these hyperelastic materials through FE analysis, the Mooney-Rivlin model is adopted on the polynomial development of total strain energy. The Mooney-Rivlin material model has previously been used to successfully predict the behaviour of PE. The Mooney-Rivlin strain energy potential is adopted as follows [46]:

$$\sigma_{ij} = \frac{\partial W}{\partial \varepsilon_{ij}} \tag{13}$$

$$W = \sum_{k+m=1}^{n} C_{km}(I_1 - 3)^k + (I_2 - 3)^m + \frac{1}{2}k(I_3 - 1)^2$$

where W is the strain energy per unit of reference volume while I_1, I_2, I_3 are the strain variants. k is the bulk modulus and I_3=1 for incompressible material behaviour; C_{km} is the constant of the Mooney-Rivlin material. Two Mooney-Rivlin parameters (C_{10} and C_{01}) given in Table 2 are often used to describe the hyper-elastic rubber deformation.

The input parameters defined in the *MAT_PLASTIC-KINEMATIC model are based on quasi-static material testing. The strain rate effect is taken into consideration by using the Cowper-Symonds model whose equation is given as:

$$\frac{\sigma_d}{\sigma_s} = 1 + \left(\frac{\dot{\varepsilon}}{C}\right)^{1/p} \tag{14}$$

where σ_d and σ_s are the dynamic yield stress and the static yield stress at the plastic strain rate $\dot{\varepsilon}$, respectively. The constant strain rate parameters are expressed by Cowper C and Symonds P.

Table 2. Material properties in the numerical model

Category	Material models	Parameters	Value
Al 1060 [31]	MAT_JOHNSON_COOK	Density	2770 kg/m^3
		Poisson's ratio	0.33
		Young's modulus	70 GPa
		Yield stress A	0.369 GPa
		Hardening constant B	0.675 GPa
		Strain rate constant C	0.007
		Thermal softening exponent m	1.5
		Hardening exponent n	0.7
		Melting temperature T_m	800 K
		Ref. strain rate $\dot{\varepsilon}_0$	1.0 (s^{-1})
Lead [47]	MAT_PLASTIC_KINEMATIC	Density	11,400 kg/m^3
		Poisson's ratio	0.44
		Young's modulus	16 GPa
		Yield stress	20 MPa
		Tangent modulus	50 MPa
		Hardening parameter	10^9
		Strain rate parameter C	10^9
		Strain rate parameter P	1

		Failure strain	0
PU [48]	MAT_MOONEY_RIVLIN_RUBBER	Density	900 kg/m^3
		Poisson's ratio	0.42
		Constant C_{10}	21.5 MPa
		Constant C_{01}	4.3 MPa

Table 3. Equation of state for aluminium [45]

C_0 (Pa)	C_1 (GPa)	C_2 (GPa)	C_3 (GPa)	C_4	C_5	C_6	E_0 (GPa)	V_0 (m^3/m^3)
0	74.2	60.5	36.5	1.96	0	0	0	1

4.1.2 *Modelling contacts and boundary conditions*

The model utilized to simulate the contact between the impactor and top facesheet of the panel is applied by the card *AUTOMATIC_SURFACE_TO_SURFACE while the contact definition between the metals and polyurethane is *TIED_SURFACE_TO_SURFACE to assume their perfect bond. Since it is assumed that the interfaces between PU and the metals of the meta-panel are perfectly bonded, hence no debonding analysis is carried out. Besides, the card *TIED_NODE_TO_SURFACE is adopted to simulate the joint between the facesheets and the meta-truss bars. All nodes along the perimeter of the bottom facesheet are fixed in all directions using the *BOUNDARY_SPC_SET. In this study, solid hexahedron elements (SOLID 164) are utilized to model all the elements. LS-DYNA provides two types of bulk viscosity coefficients namely Q_1 and Q_2 to treat shocks. While Q_1 helps to smear the shocks and also prevents the element from collapsing under high velocities, Q_2, called as a linear term, helps to rapidly damp out the oscillations. By default, these coefficients are fixed at Q_1=1.5 and Q_2=0.06 and both are active for solid elements in this study [49]. The gradient mesh size is employed after conducting a mesh size sensitivity analysis which will be presented in Section 4.2.

4.1.3 *Impactor*

The steel impactor is modelled as a rigid body. The impactor has a spherical shape of 20 mm radius and its weight is 1 kg. The initial velocity of the impactor against the panel is 3 m/s and is defined by the *INITIAL_VELOCITY_GENERATION card, which is applied to all nodes of the impactor. The predicted impact force-time history is shown in Fig. 5(a) while Fig. 5(b) depicts the corresponding FFT spectrum. As shown, the peak impact force is nearly 10 kN with the dominant frequencies of impact loading up to approximately 3,000 Hz.

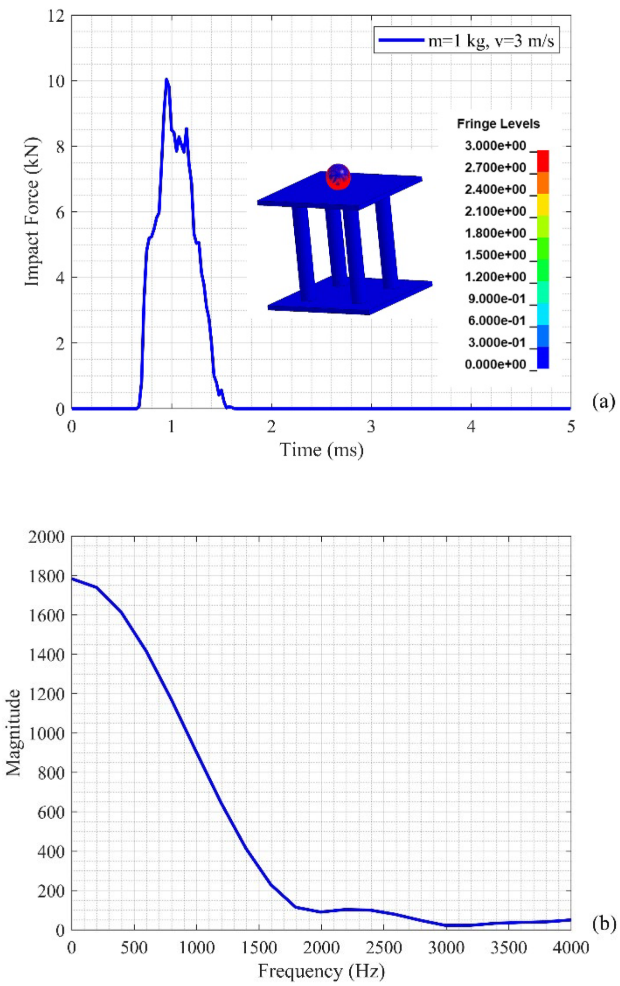

Fig. 5. (a) Time history of impact force and (b) frequency domain.

4.2 Mesh convergence study

Typically, to secure the accuracy of the numerical simulations, a mesh convergent study is conducted by varying mesh sizes, i.e. 3 mm, 2 mm, 1 mm, 0.5 mm, and gradient mesh which represents coarse, medium, and fine meshes. Fig. 6(a) shows the schematic diagram of gradient mesh sizes for the meta-panel, in which a uniform mesh size of 1 mm is adopted for the meta-truss bar while for the facesheets, the mesh sizes of 0.5 mm and 1 mm are set for the impact area (60 x 60 mm^2 in the centre area) and the remaining area, respectively. The central point displacement of the top facesheet of the meta-panel and the computational cost corresponding to various mesh sizes are shown in Fig. 6(b). As observed, the mesh size of 0.5 mm and gradient mesh result in similar outcomes. The mesh size is considered to converge at about 0.5 mm while its computational cost is greatly higher than that of the gradient mesh sizes. Therefore, the gradient mesh size is utilized in the subsequent numerical simulations when considering both the accuracy and efficiency.

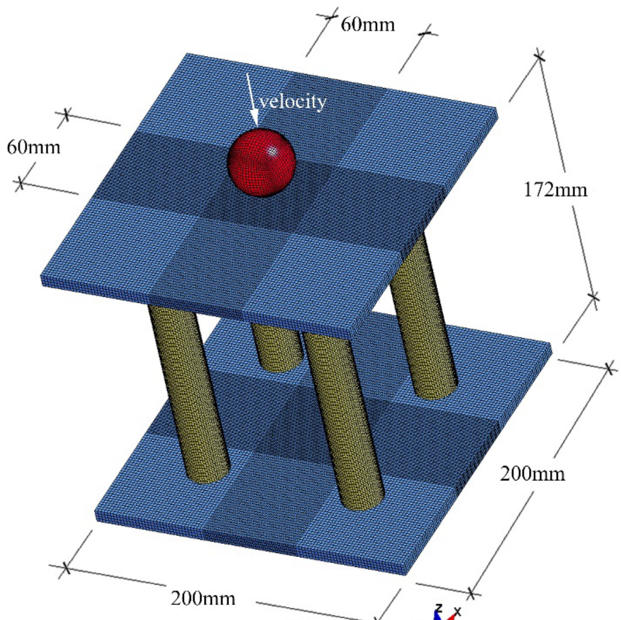

(a)

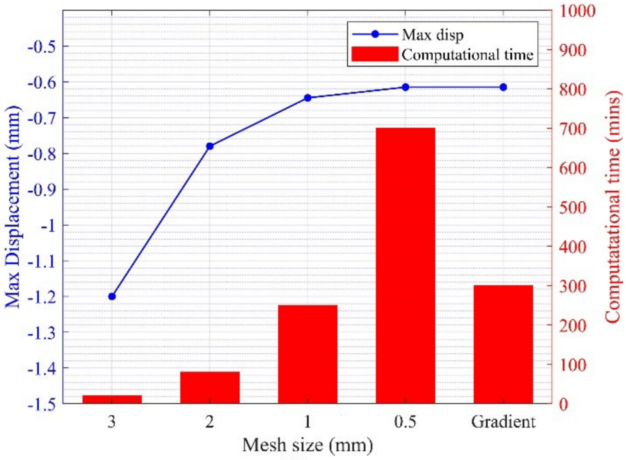

(b)

Fig. 6. Mesh convergence analysis (a) FE model and (b) mesh sensitivity.

4.3 Model validation

The transmission coefficient from both numerical and analytical derivation is utilized for model validation. One end of the meta-truss bar is excited by the input signal in a form of prescribed displacement with a sweep frequency of [0 – 20,000] Hz while the output response is captured at the other end to calculate the transmission coefficient. It is worth mentioning that the prescribed displacement is generated by the sweep-frequency cosine function named “Chirp” in Matlab. Then, it is applied to the meta-truss bar model in Ls-Dyna using the keyword *PRESCRIBED_MOTION_SET. As shown in Fig. 7, the numerical and the theoretical transmission coefficients are in good agreement, implying the validity of the model. For the numerical simulation, the frequency ranges of [0 - 3,600] Hz and [>9,000] Hz are respectively the 1st and the 2nd bandgap while the corresponding regions of the bandgap from the theoretical results are [0 - 3,500] Hz and [>9,500] Hz as presented above. It is observed that there are some slight discrepancies between the two approaches. This is because, as discussed above, the assumption of the infinite number of cells in the theoretical derivation of the meta-truss bar, while in the numerical model only a finite length of the meta-truss bar is modelled. Furthermore, boundary reflections of the wave propagating in the finite length truss bar also affect the numerical results.

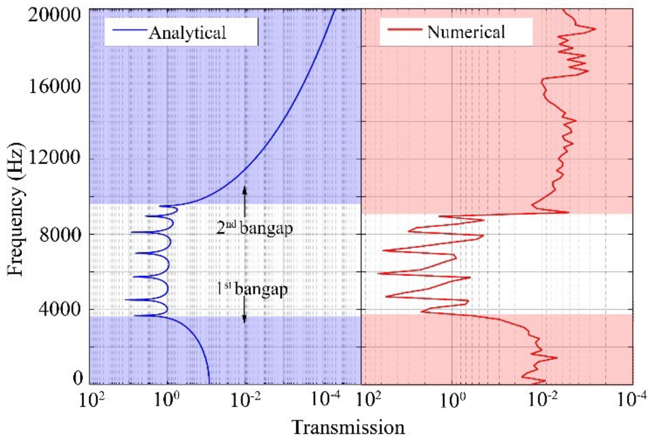

Fig. 7. Analytical and numerical transmission coefficients of the meta-truss bar.

To further validate the numerical simulation, a prescribed displacement with multi-frequency components [50] is excited at one end of the meta-truss bar (as shown in Fig. 2(b)) to verify its frequency suppression capacity as follows:

$$u(t) = 10^{-4} \sum_{n=1}^{3} sin[2\pi f_n t] H(t) \tag{15}$$

where $H(t)$ is the unit-step function and given as

$$\mathrm{H}(t) = \begin{cases} 1, t \geq 0 \\ 0, t < 0 \end{cases} \tag{16}$$

and f_n = [200; 1,000; 6,000] Hz, n = 1, 2, 3, respectively. The frequencies f_1 and f_2 are purposely chosen at low frequencies which are often in the frequency range of impact loading and also fall into the bandgap of the meta-truss bar while f_3 is within its passband as shown in Fig. 7. The input and output signals are compared by the displacement-time histories and the FFT spectra, which are shown in Fig. 8 and Fig. 9, respectively. It is found that only the frequency of 6,000 Hz can travel through the meta-truss bar whereas the frequencies of 200 Hz and 1,000 Hz, which fall into its bandgap as shown in Fig. 7 are completely suppressed. These results indicate the filtering capacity of the meta-truss bar with frequencies falling in its bandgaps. In summary, by introducing meta-cores inside the hollow truss bar, frequency bandgaps can be generated to effectively filter out stress waves propagating through the meta-lattice truss bar.

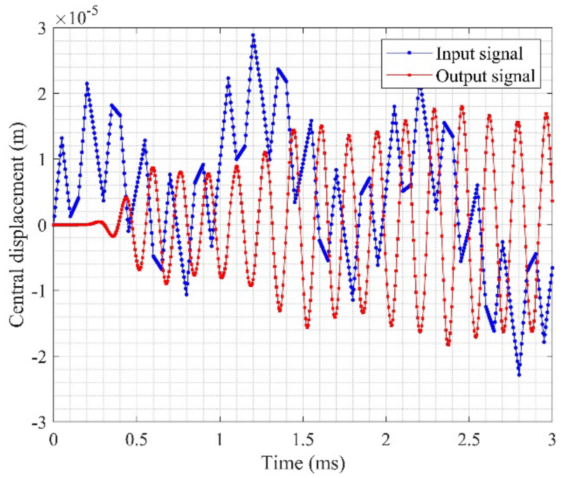

Fig. 8. Displacement-time histories at the center points of the meta-truss bar.

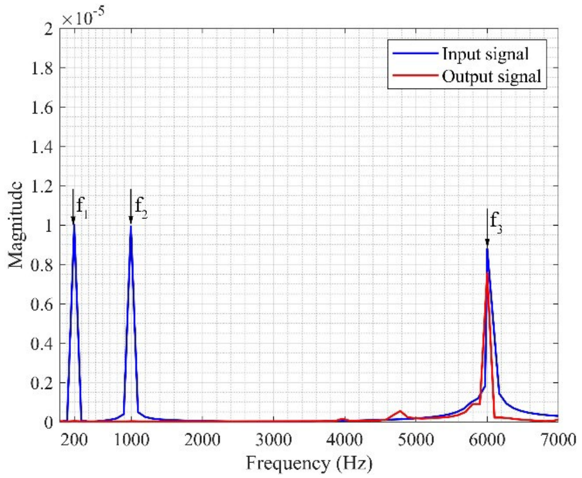

Fig. 9. FFTspectra of the displacements at the center points of the meta-truss bar.

4.4 Results and discussions

The numerical model of the meta-panel (shown in Fig. 2) is developed by using the explicit finite element code LS-DYNA in this subsection to demonstrate its structural performance in withstanding impact loading. Two conventional panels comprising solid bars and hollow bars as respectively shown in Figs. 10(a) and 10(b) are built for comparison. These panels are intentionally designed with the same geometric parameters as the meta-panel, and the only different component among them is the truss-cores connecting two facesheets. Specifically, the solid-truss bar, hollow-truss bar, and meta-lattice truss bar have the same diameter. In this study, the main aim is to examine the dynamic behaviour of the meta-truss bar in attenuating the impact load, therefore, the truss bar size remains the same instead of making the same weight due to two reasons. Firstly, if the hollow truss bar thickness and/or diameter is tailored to have a similar mass as the solid bar, its size could be very large which also influence its deformation and hence energy absorption. Secondly, to maintain the same weight, diameters of the solid truss and hollow truss bar have to be greater than the meta-truss bar due to the higher density of lead core than the aluminium core. This results in decreasing energy absorption of these panels. Therefore the same size of the three sacrificial panels is considered in the analysis in this study. The structural responses including the central displacement of the facesheets, the reaction force-time history, and energy absorption are evaluated among these three panels to validate the effectiveness of the meta-panel in mitigating the impact loading effects, which is described in Section 4.1.3.

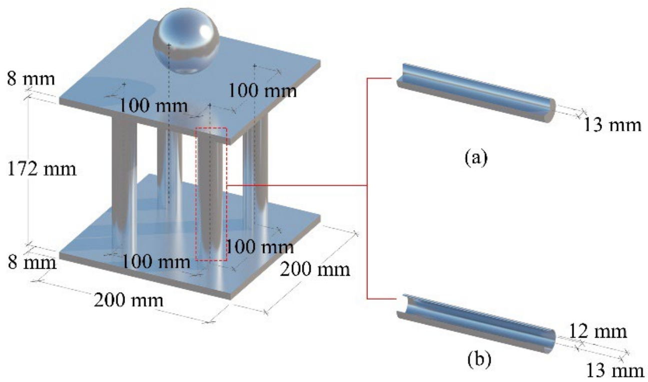

Fig. 10. Schematic diagram of panels comprising of (a) solid truss bar and (b) hollow truss bar.

4.4.1 *Deformation analysis*

Figs.11 (a), (b), and (c) show the displacement contours of the bottom facesheet of the panels with solid truss bars, hollow truss bars, and meta-truss bars, respectively, and Fig. 12 (a) shows the displacement-time histories at the center of the bottom facesheet of the three panels. As shown in Fig. 12 (a), the meta-panel has a similar deformation pattern with the other two reference panels due to their similar configurations, but smaller maximum displacement at the bottom facesheet than the other two referenced panels. As indicated in Fig. 11, the maximum displacement of the meta-panel is 0.31 mm, which is 20% and 33% lower than those of the panel with hollow-truss bars and solid-truss bars, respectively. This is because the vibration of meta-cores, which generates bandgaps and filters the incident waves within its bandgaps, result in lower impulse transferring to the bottom facesheet of the panel. The FFT spectrum of displacement response of the three panels is illustrated in Fig. 12 (b). For the meta-panel, a reduction of the peak amplitude of the central displacement occurs in the 1st bandgap around 0 – 3,500 Hz, which well agrees with the prediction in Section 3. However, as can be noted, unlike those shown in Fig. 9, only partial incident wave is mitigated within the bandgap, i.e., wave energy is still transmitted in the bandgap of the meta-panel although some reductions are observed as compared to the other two reference panels. This is because only a portion of the incident wave propagates through the meta-core and thus is mitigated while other portions of wave energy travel through the outer tube of the truss bars. In the above section 4.3, the incident displacement is only applied to the core so that it is completely filtered within the bandgap while in the meta-panel, it is a combination of three components, i.e, the facesheets, the truss bars, and the meta-cores and only the meta-core has bandgaps to filter out wave energy. In general, the meta-panel has a smaller deformation compared to its conventional counterparts, indicating its effectiveness in mitigating the impact loading effect for structure protection.

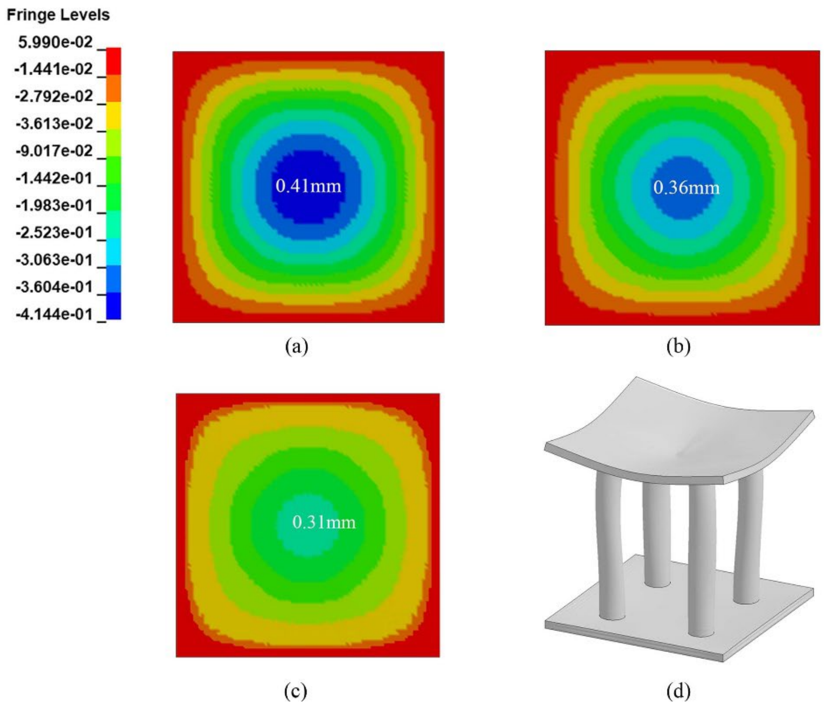

Fig. 11. Displacement contour of the bottom facesheets (a) solid-truss panel, (b) hollow-truss panel, (c) meta-panel, and (d) deformation pattern of the meta-panel.

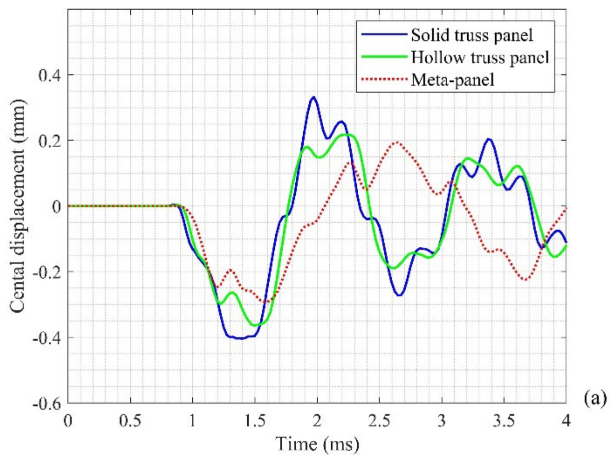

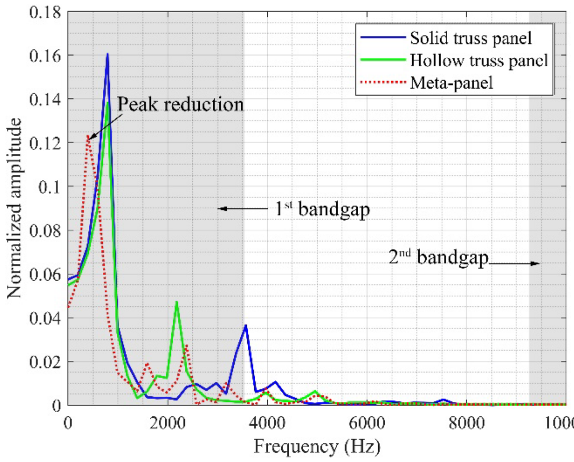

(b)

Fig. 12. Displacement at center of the bottom facesheet of the three panels (a) time histories, (b) frequency spectra.

4.4.2 Energy absorption characteristics

To obtain an inclusive comprehension of its impact mitigation, analysis on the energy absorption capacity of the meta-panel subjected to impact loads are conducted. Fig. 13(a) shows the total energy while Figs. 13 (b) and (c) exhibit the kinetic energy, and the internal energy absorbed by each constituent of the meta-panel under impact loads, respectively. As shown, due to the existence of the soft coating, there is a relative movement between the lead cores and the aluminium tube which absorbs a significant amount of energy. This movement is observed because, as shown in Fig. 13(a), when the energy absorption by the coating and the core increases to a peak value, the energy in the truss bars is at its minimum. This effect is very obvious at a late stage when t is larger than about 1.5 ms as shown in the figure. At the beginning of the impact, the energy absorbed by the core is relatively small since it takes time for the cores to be activated. The obtained findings reveal the damage mitigation effect to the truss bars by the impact load due to the local vibrations of the meta-cores which absorb energy. As shown in Fig. 13 (c), the hollow tube deformation contributes significantly to the internal energy of the meta-panel, while the motions of the meta-cores result in a significant amount of kinetic energy

(Fig. 13 (b)) and partially to the small internal energy through the elastic deformation of the coatings (Fig. 13 (c)). It is worth mentioning that the initial energy of the impactor is 4.5 J and entirely in the kinetic form before the impact with the velocity of 3 m/s. At 1.2 ms when the velocity of the impactor equals 0, it changes direction, implying the deformation of the meta-panel at the maximum value and the impactor starts to rebound. After the impact at around 1.5 ms, the velocity of the impactor slightly reduces but the change is very small due to the extremely short duration of the impact event so that the residual velocity looks constant. In general, these findings indicate that the meta-panel utilize a coupled mechanism of energy absorption by combining the local resonance of the meta-cores and deformation of the outer hollow tubes, leading to a high energy absorption capacity.

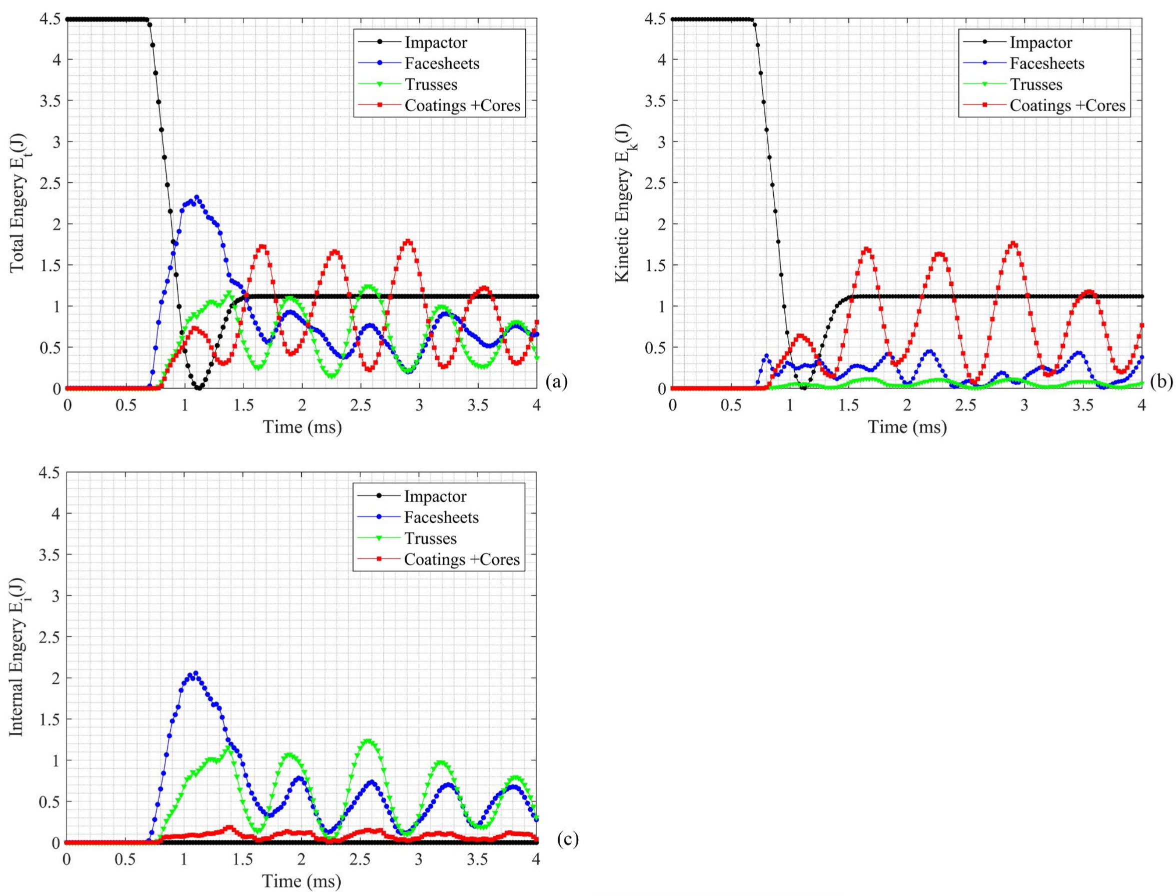

Fig. 13. (a) Total energy distribution of meta-panels, (b) kinetic energy, and (c) internal energy.

Fig. 14 depicts the total energy absorption of the three panels and each constituent in these panels to evaluate the effectiveness of the meta-panel. As shown, the total energy absorption of the meta-panel is the highest among these considered panels, indicating that the meta-panel has more advantages in terms of energy absorption capacity. This is because the meta-panel absorbs energy through the truss bars and the facesheets deformation, combined with local resonant of the lead cores while both the reference panels absorb energy only through plastic deformation of the truss bars and the facesheets. Compared to other truss elements, the solid truss bar panel absorbs the least energy due to less deformation, implying the least protective performance. Conversely, the energy absorbed by the hollow truss bars is the largest compared to other panels, implying its largest plastic deformation. It is worth mentioning that although the total energy absorption of the meta-panel is higher than the reference panels, the energy absorbed by the facesheets is the smallest, indicating less damages to facesheets and outside hollow truss bars. Therefore, the thickness of the facesheets and the hollow tubes of the meta-panel could be reduced to absorb the same amount of energy compared to the referenced panels, meaning less material consumption on the facesheets and the truss bars of the meta-panel. The above findings further exhibit the superiority of the meta-panel in impact resistance.

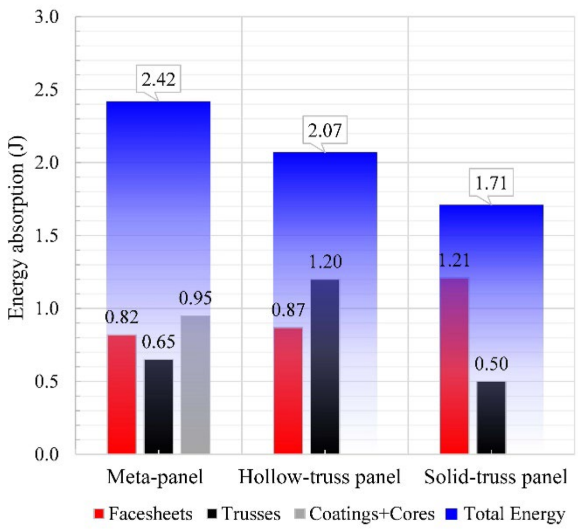

Fig. 14. Energy absorption of the three panels.

4.4.3 *Reaction force and Von Mises stress response*

The objective of utilizing sacrificial cladding is to mitigate the impact load and reduce the transmitted force to the protected structures. The transmitted force-time history is obtained from the numerical simulation by plotting the reaction force exerted on the base of the structure. The cumulative reaction force around the boundary of the bottom facesheet is set as a main criterion for the evaluation and is taken as the sum of nodal forces distributed around the boundary. As shown in Fig. 15 (a), the peak value of reaction force to the base structure from the meta-panel is respectively 46.7% and 33.4% less than the corresponding of other panels with hollow truss and solid truss, indicating its effectiveness in reducing the transmitted force to the base structure under impact loads. It can be attributed to the fact that the movements of the resonator and the soft coating generate the bandgap which can filter out the stress from the impact load, resulting in a reduction in stress transmission from the impact load to the bottom facesheet and then the supports. Furthermore, spectrum analysis of reaction forces in the frequency domain of the three panels is illustrated in Fig. 15 (b). As shown, a clear reduction of the peak amplitude of the reaction force of the meta-panel is observed in the 1st bandgap of 0 – 3,500 Hz, but the reaction force in this frequency band is not completely suppressed because the outer tube of the truss bars can transmit a certain amount of impact load as discussed above. Overall, the meta-panel outperforms the other two reference cladding panels by yielding a smaller reaction force which demonstrates its superiority over the two reference panels.

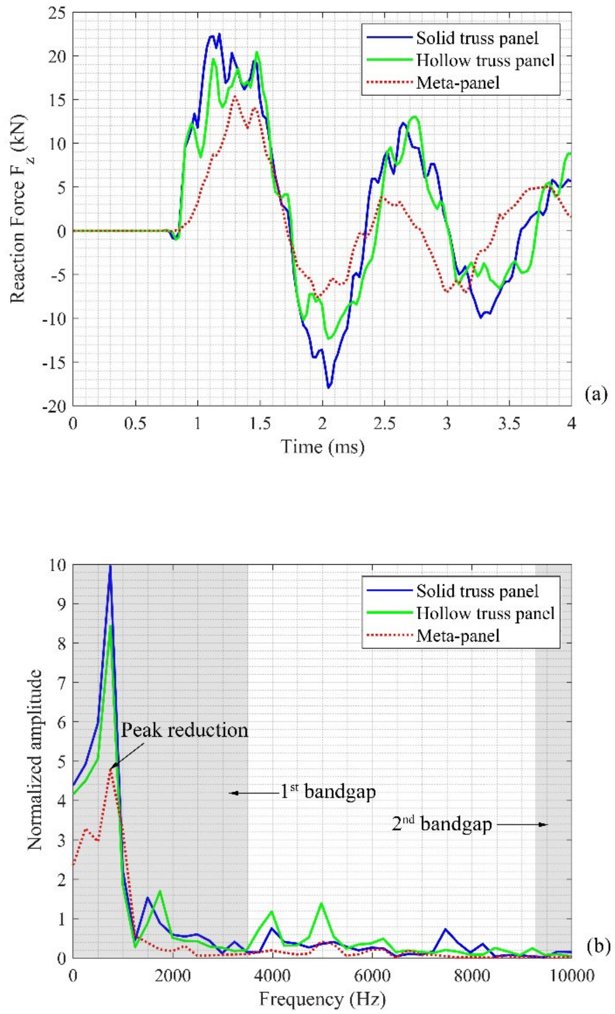

Fig. 15. Reaction force of the three panels under impact loading (a) time histories, (b) frequency spectra.

To obtain a better realization of the working mechanism, the von Mises stress distribution occurring at the bottom facesheet is also used. The stress contours at bottom facesheets of all considered panels are shown in Fig. 16. It is clear from the figure, the stress distribution is similar for all the panels, and stress is concentrated at the connections between the cores and the facesheets. The results also show that the bottom facesheet of the meta-panel experiences the smallest von Mises stresses among the considered panels, followed by the hollow truss panel solid truss panels, respectively. This means that the stresses transferred to the bottom facesheets are effectively mitigated by the meta-cores, implying the superior performance of the meta-panel in terms of the stress wave mitigation capability.

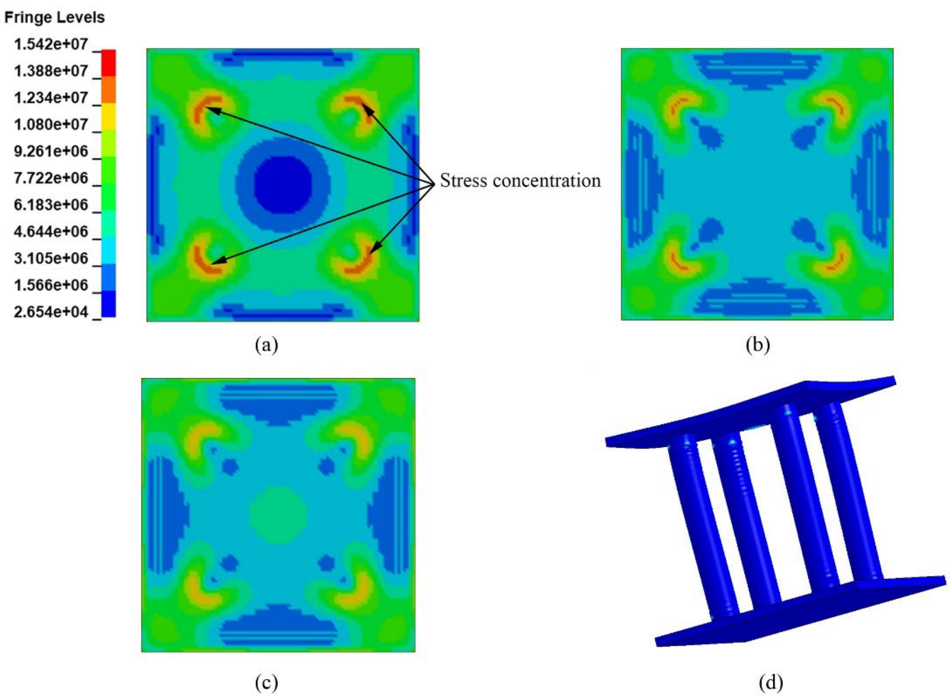

Fig. 16. Von Mises stress contours at the bottom facesheets of the investigated panels (a) solid-truss panel, (b) hollow-truss panel, (c) meta-panel, and (d) plastic deformation of the meta-panel.

4.5 Parametric studies

The above finite element model of meta-panel is employed in this section to investigate the effects of the crucial factors, e.g., the truss bar thickness, meta-core properties, and impact velocity on its transient responses under impact loading.

4.5.1 *Effect of the truss bar thickness*

To examine the influence of the thickness of the truss bar in the meta-panel, four different truss bar thicknesses, i.e. 4 mm, 3 mm, 2 mm, and 1 mm, with the same inner diameter of 24 mm (Fig. 17) are considered. While the truss thickness is varied, other dimensions of the meta-panel and the impactor (Section 4.1.3) are kept the same in this investigation.

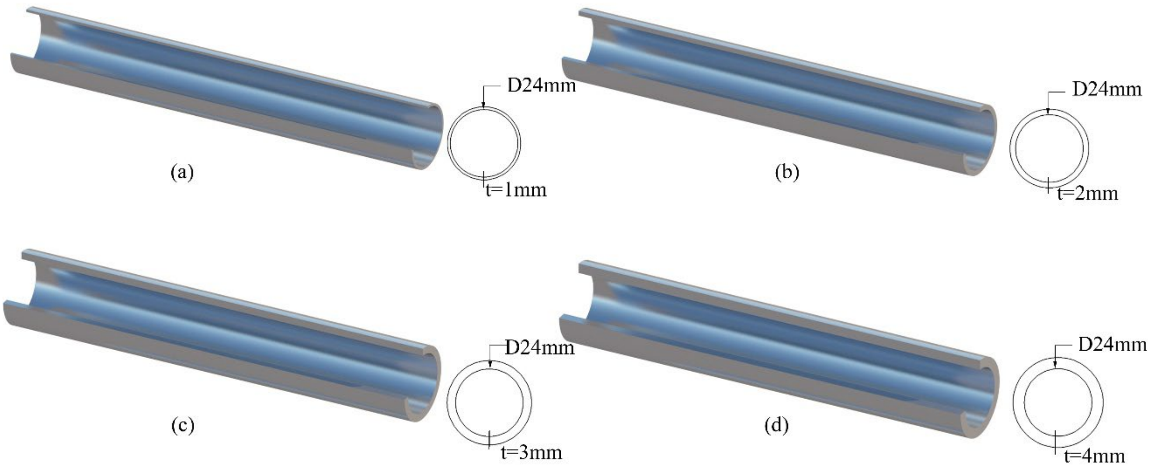

Fig. 17. Schematic diagram of various thickness configurations of the meta-lattice truss bar.

Figs. 18 (a) and (e) show the comparison of the bottom and top facesheet deflection of meta-panel with varying truss thicknesses, respectively. As expected, there is a slight decrease in the central deflection of the top facesheet while that of the bottom facesheet increases with the increased thickness of the truss bar. This is because the ratio of stress propagating through the hollow truss bar and the meta-core in the meta-truss bar critically relies on the ratios of the cross-sectional area and stiffness. Increasing the thickness of the truss bar leads to less stress waves from the impact load propagating through the meta-core, implying less efficiency of the meta-panel. A significant reduction in the displacement of the bottom facesheet by decreasing the truss tube thickness proves its impact mitigating effect. As observed in Figs. 18 (c) and (f), the reaction force increases with the thickness of the truss bar increasing from 1 mm to 4 mm while there is a substantial reduction of the total energy absorption, accordingly. This is attributed to the fact that the less deflection of the facesheets and deformation of the truss bar, indicating less energy absorption through their plastic deformations as well as fewer stress waves passing through the meta-core, meaning less conversion of impact energy to the kinetic energy of the meta-core. The FFT spectrum of displacement and reaction force of the three panels are illustrated in Figs. 18 (b) and (d). For the meta-panel, a reduction of the peak amplitude of the central displacement and reaction force occurs in the 1st bandgap at approximately 0 – 3,500 Hz, which well agrees with the prediction in Section 3. In summary, the reaction force, which is a critical criterion in designing sacrificial claddings, is significantly affected by the truss thickness and it is suggested to utilize a thin truss bar in practice. Therefore, the recommended configuration of the meta-panel should possess a relatively thin truss bar to fully leverage its protective performance as a sacrificial cladding.

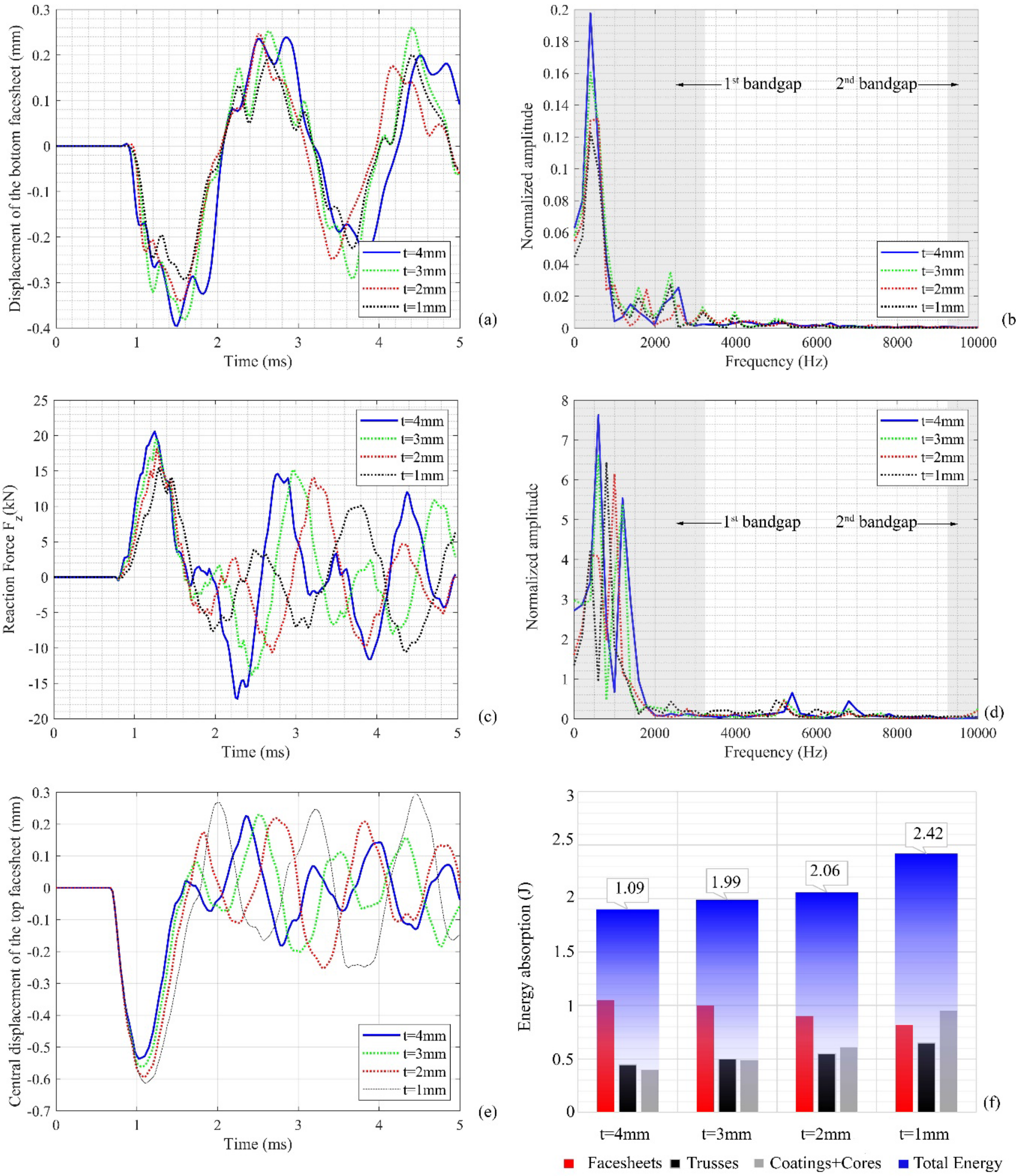

Fig. 18. Effects of the truss bar thickness (a-b) displacement of bottom facesheet in time histories and FFT spectra, (c-d) reaction force in time histories and FFT spectra, and (e-f) displacement of top facesheet and energy absorption.

4.5.2 *Effects of meta-core properties*

The influence of the meta-core properties including coating modulus (E_c) and core density (ρ_c) on the dynamic responses of the meta-panel under impact loads are examined in this section. The geometry of the panel and the impactor used in this section is the same as in Section 2 and Section 4.1.3.

4.5.2.1 Effect of coating modulus (E_c)

To investigate the effect of the stiffness of the soft coating on the impact mitigating behaviour of the meta-panel, the coating modulus of E_{c1}=1.47x10^1 MPa, E_{c2}=1.47x10^2 MPa, E_{c3}=1.47x10^3 MPa are considered, which represent very soft, medium, and hard polyurethane materials [33]. In this section, only the soft coating modulus of the meta-core is changed while all other parameters are kept the same as defined in Section 2.

The displacement and velocity-time histories of core 1 with different Young's modulus of the coating are respectively shown in Figs. 19 (a) and (c) while their corresponding dominant frequencies are depicted in Figs. 19 (b) and (d). It is observed that the smaller the coating modulus, the larger displacement of the lead core would be. It is because the role of the soft coating in the meta-core is to allow relative movement of the lead core, accordingly, it would be easier to vibrate in the softer coating. Fig. 20 (f) depicts the energy absorption of each constituent in the meta-panel corresponding to the three elastic moduli of the soft coating. It is seen that the lead core has the highest energy absorption when E_{c2}=1.47x10^2 MPa although the displacement of core 1 with E_{c1}=1.47x10^1 MPa is the largest among all considered cases. This is attributed to the fact that with the very soft coating, the energy transmitted to the core is small even though the movements of the cores are ample but their vibrations are more slowly compared to the case with medium elastic modulus. On the other hand, with the very hard coating, i.e., E_{c3}=1.47x10^3 MPa, the core is difficult to vibrate and the displacement of core 1 is relatively small, leading to small energy absorption by the meta-core. Hence, to obtain the optimal performance of the meta-core of the meta-panel in mitigating impact loading, it is necessary to carry out proper analysis to determine the optimal elastic modulus of the soft coating. The best performing soft coating in this study is a polyurethane (PU) with an elastic modulus of 1.47x10^2 MPa. This result is consistent with other meta-related structures such as metaconcrete [33].

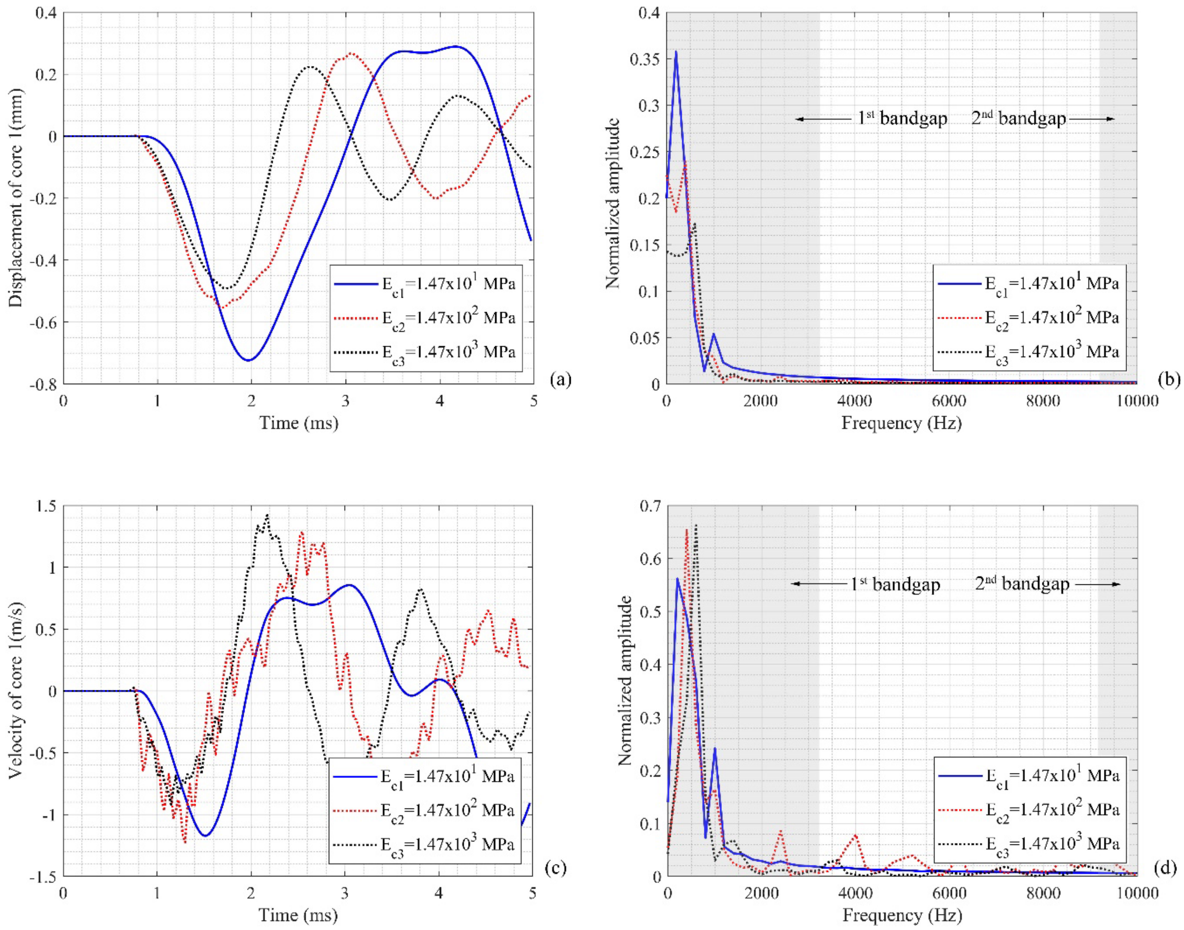

Fig. 19. Dynamic responses of core 1 (a-b) displacement of core 1 in time histories and FFT spectra, and (c-d) velocity of core 1 in time histories and FFT spectra.

When changing the coating elastic modulus, the displacement of the top facesheet of the meta-panel is the same initially but becomes different subsequently as shown in Fig. 20 (e). This is because the stress waves induced by the impact loading propagate orderly from the top facesheet to the bottom facesheet. Irrespective of the coating modulus, the top facesheet always resist the impact loading firstly, therefore, its displacement is not affected by the coating modulus of the meta-truss bars. Nonetheless, the top facesheet displacement becomes different after the first peak response because changing the coating stiffness is equivalent to changing the supporting stiffness of the top facesheet, and the supporting stiffness influence vibration responses of the facesheet. As shown in Figs. 20 (a) and (c), the smallest displacement at the bottom facesheet and the reaction force is observed when the coating elastic modulus is medium while the very soft and very hard coating is less effective in mitigating the stress wave propagation from the impact loading. The FFT analysis of displacement and reaction force response shown in Fig. 20 (b) and (d) indicates a reduction of the peak amplitude of the central displacement and reaction force that occurs in the predicted bandgap. These results, again, indicate that a properly selected elastic modulus of the meta-panel is necessary to achieve its optimal performance in mitigating the impact loading effect.

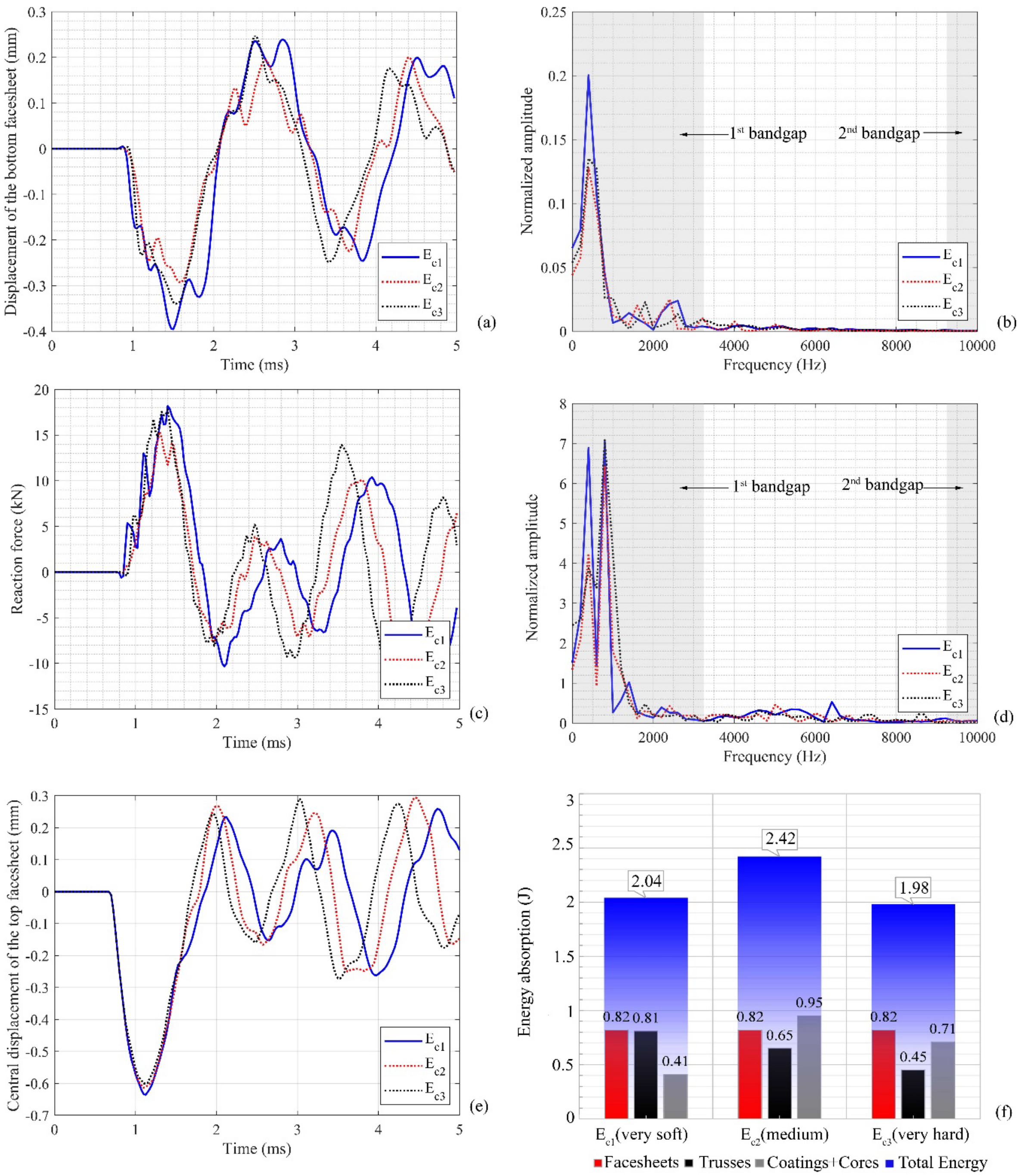

Fig. 20. Effects of the coating modulus (a-b) displacement of bottom facesheet in time histories and FFT spectra, (c-d) reaction force in time histories and FFT spectra, and (e-f) displacement of top facesheet and energy absorption.

4.5.2.2 Effect of core density (ρ_c)

To investigate the influence of the core density on the performance of the meta-panel, three core material densities, i.e, ρ_{c1}=11,400 kg/m^3, ρ_{c2}=7,850 kg/m^3, and ρ_{c3}=2,770 kg/m^3, which correspond to lead, steel, and aluminium, respectively, are considered herein. Other parameters such as the geometries of the panel and the impactor used in the model are the same as those defined above.

Fig. 21 depicts the transmission coefficient of the meta-lattice truss bar when the core densities are different. As shown, the region of the passband which is the range of frequency where the stress wave can propagate through becomes wider with the decreasing core density. In other words, the heavier the density of the core is, the narrower passband the meta-lattice truss bar would have, implying the more effective of the meta-panel. For instance, the passband width changes from [3,500 - 9,500] Hz to [7,500 - 19,000] Hz by changing ρ_{c1} to ρ_3, while the frequency passband of the case ρ_{c2} is [4,600 - 12,000] Hz. The reason causing changes in the passband range is that increasing the core density increases the mass of the core, resulting in a decrease in the upper bound frequency of the 1st bandgap and an increase in the lower bound frequency of the 2nd bandgap, which leads to a narrower passband width as shown in Fig. 21. Therefore, it can be concluded that the passband of the meta-lattice truss bar is sensitive to the variation of the core density and it decreases with the rising core density when the core size and the coating are unchanged. However, it is observed from Table 4 that the transient responses of the meta-panel are not prominently affected by the considered core densities. It is because although there is an increase in the bandgaps of the meta-core when increasing the core density, the dominant frequency of the impact loading as described in Fig. 5 ranging from [0 - 3,000] Hz falls in the 1st bandgap of all the considered cases. In general, increasing the core density results in a narrower 1st bandgap but a broader total region of the bandgap range of the meta-core while it has a limited effect on the transient performances of the meta-panel within the studied range of impact loading.

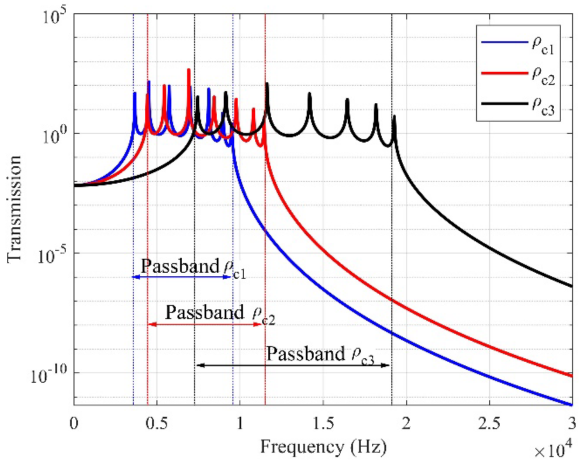

Fig. 21. Transmission coefficients of the meta-truss bar with different core densities.

Table 4. Effect of core density on displacements, reaction force, and energy absorptions.

Core density	Displacement (mm)		Reaction force (kN)	Energy absorption (J)			
	Top facesheet	Bottom facesheet	F_z	Facesheets	Truss bars	Coating + Core	Total
ρ_{c1}	0.61	0.32	15.0	0.82	0.65	0.95	2.42
ρ_{c2}	0.61	0.33	15.3	0.82	0.65	0.91	2.38
ρ_{c3}	0.61	0.34	15.4	0.82	0.65	0.87	2.34

4.5.3 *Effect of impact velocity*

As reported in previous studies [51, 52], the impact velocity has a significant influence on the performance of the sandwich panels. Therefore, a parametric study of the influence of the impact velocity on the responses of the meta-panel is conducted. In this study, the impact is performed by an impactor having the same mass but different velocities resulting in different impact energies.

To comprehend the influence of different levels of impact velocity on a given meta-panel, four impact scenarios with various velocities but the same mass are considered. The range of impact energy levels is attained by utilizing four different impact velocities, i.e. v_1=1 m/s, v_2=5 m/s, v_3=20 m/s, and v_4=30 m/s with a constant impactor mass of 0.5 kg. The corresponding impact energies are 0.25 J, 6.25 J, 100 J, and 225 J, respectively.

As shown in Fig. 22 (a), increasing impact velocity results in a higher impact force peak, but has limited influence on the duration of the impact loadings [53]. It should be noted that although the dominant frequencies of the impact forces of the considered examples are still in the 1st bandgap of [0 - 3,000] Hz, increasing impact velocity results in more impact force energies in the higher frequency range that fall into the passband of the meta-panel (Fig. 22 (b)). The impact energy in the bandgaps of the investigated meta-truss bar is determined by the shaded area (A_{bandgap}) as shown in Fig. 22 (b) enclosed by the FFT spectrum. Besides, Table 6 gives the impact energy percentage corresponding to each bandgap which is estimated by the ratio between the energy in each bandgap and the total impact energy (A_{total}). It is found that the impact load with lower velocities leads to more percentage of energy in the bandgaps, i.e, 100.0%, 80.9%,75.5%, and 70.2% respectively for the loadings v_1 to v_4, indicating the meta-panel is less effective in alleviating the impact load-induced from the high velocity.

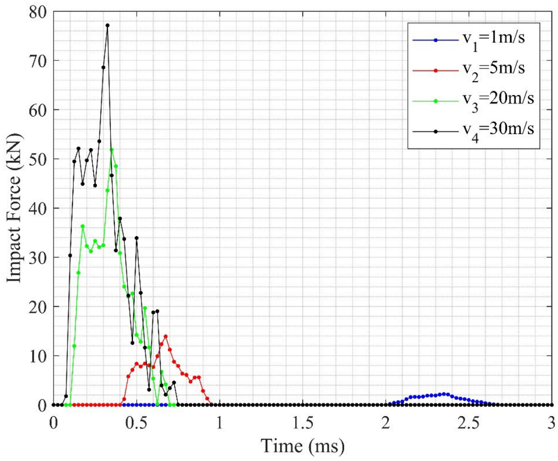

(a)

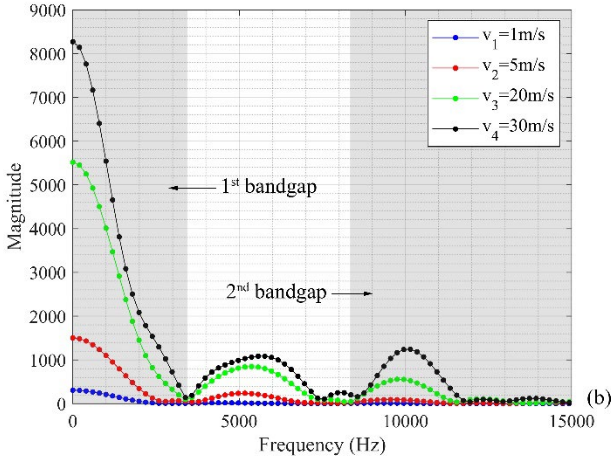

Fig. 22. Impact loading with various velocities, (a) time-histories, and (b) FFT.

The structural responses of the meta-panel under impact loads with various velocities are given in Table 6 while Fig. 23 depicts the deformation contour of the meta-panel with various velocities. As shown, transient behaviour of the meta-panel depend on the impact loading impulse and the frequency band structure. Specifically, rising the loading impulse leads to the increase of the facesheet displacements, the energy absorption, and the reaction forces of the meta-panel. The case with velocity v_1 corresponds to the highest proportion of impact energy being absorbed by the coating and the core at 0.045/0.121=37.1% of the total energy as shown in Table 5, followed by 34.6%, 30.9%, and 28.7% respectively for the impact case with velocity v_2, v_3, and v_4 even though there is an increase in the total energy absorbed owning to the increased impact energy from v_1 to v_4. This is attributed to the decrease in the proportion of the impact energy from case v_1 to case v_4 falling in the bandgap of the meta-panel, indicating the more percentage of the impact loading falling in the bandgaps, the more effective of the meta-panels in impact mitigation performance.

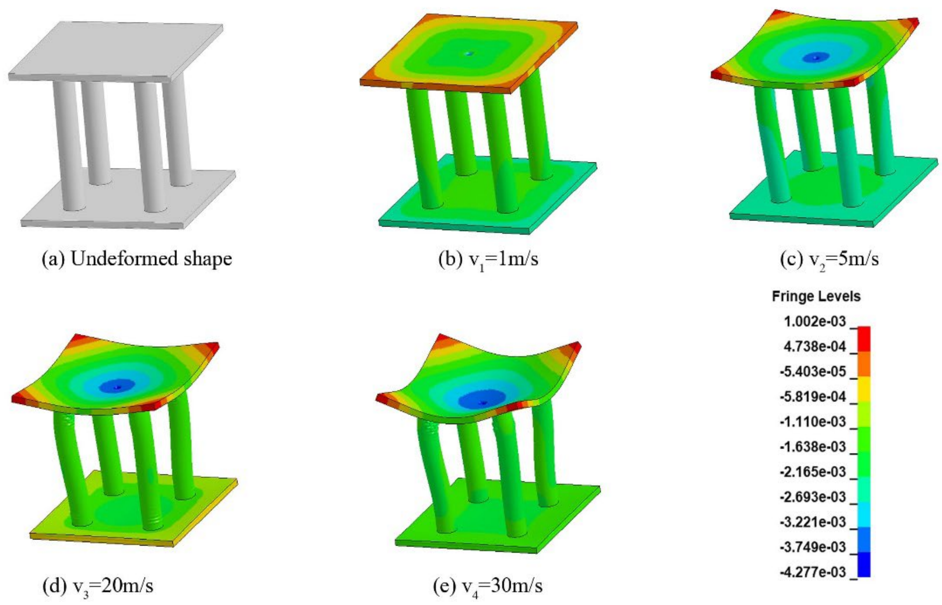

Fig. 23. Undeformed and deformed contour of the meta-panel under impact with various velocities.

Table 5. Proportion of impact energy with various velocities in the bandgaps.

Impact velocity	1st bandgap		2nd bandgap		Total
	$\frac{A_{\text{bandgap}}}{A_{\text{total}}}$	%	$\frac{A_{\text{bandgap}}}{A_{\text{total}}}$	%	%
v_1	$\frac{502{,}861}{502{,}861}$	100.0%	$\frac{0}{502{,}861}$	0.0%	100.0%
v_2	$\frac{2{,}232{,}767}{3{,}109{,}261}$	71.8%	$\frac{283{,}731}{3{,}109{,}261}$	9.1%	80.9%
v_3	$\frac{8{,}004{,}936}{12{,}410{,}755}$	64.5%	$\frac{1{,}373{,}717}{12{,}410{,}755}$	11.0%	75.5%
v_4	$\frac{10{,}410{,}843}{19{,}118{,}717}$	54.4%	$\frac{3{,}026{,}258}{19{,}118{,}717}$	15.8%	70.2%

Table 6. Effect of impact velocities on the transient response of the meta-panels.

Impact velocity	Displacement (mm)		Reaction force (kN)	Energy absorption (J)			
	Top facesheet	Bottom facesheet	F_z	Facesheets	Truss bars	Coating + Core	Total
v_1	0.14	0.11	3.0	0.046	0.030	0.045	0.121
v_2	0.67	0.34	17.5	1.210	0.830	1.080	3.120
v_3	2.61	1.33	64.4	18.38	10.90	13.15	42.43

v_4	4.01	1.86	84.8	30.48	23.69	21.81	75.98

5. Concluding remarks

In this study, the transient responses of the sandwich panel with the meta-truss core leveraging the coupled mechanisms of plastic deformation and local resonance are investigated and compared with the conventional panels with solid truss and hollow truss core. The influence of key parameters on its mitigating effectiveness under impact loads are investigated using validated numerical models. Through these investigations, the following conclusions can be drawn:

1. Compared with the solid-truss and hollow-truss panels, the meta-panel exhibits excellent impact-resistant performances. Specifically, there are considerable decreases in the peak displacement of the bottom facesheet (33%) and the reaction force (up to 47%) of the meta-panel compared to the traditional panels subjected to the same impact load.
2. Utilizing a fairly thin hollow truss bar can lead to enhanced dynamic responses of the meta-panel. The effectiveness of the meta-panel is highly sensitive to the modulus of the soft coating. The properly selected coating can lead to better energy absorption capability of the meta-panel. Also, increasing the core density can lead to a broader bandgap region of the meta-core.
3. The impact velocity significantly affects the performance of the meta-panel because it changes the primary frequency band of impact energy distribution. Increasing impact velocity results in a higher impact force peak and more impact energy distribution in the higher frequency range. The meta-panel is the most effective in mitigating the impact loading effect when the primary frequencies of impact energy fall into the bandgap of the meta-panel.

In general, the results from this study demonstrate that the meta-panel can be more effective for structure protections than the conventional claddings with hollow and solid truss cores. It has a great potential to be deployed in protective structures or energy absorbers. However, further investigations need to be carried out to study the effects of possible debonding between the soft coating and the metals, core materials, different core materials, core shapes, and coating materials on the performances of the meta-panel subjected to impact loading of different characteristics, and also to carry out laboratory and/or field tests to experimentally verify the performances of the meta-panels.

Acknowledgments

The authors would like to acknowledge the financial support from the Australian Research Council via Laureate Fellowships FL180100196. The first author also acknowledges the support through Research Training Program Scholarship (RTP) from Australian Government.

References

[1] Tran DT, Pham TM, Hao H, Chen W. Numerical investigation of flexural behaviours of precast segmental concrete beams internally post-tensioned with unbonded FRP tendons under monotonic loading. Eng Struct. 2021;249:113341.
[2] Tran DT, Pham TM, Hao H, Chen W. Numerical study on bending response of precast segmental concrete beams externally prestressed with FRP tendons. Eng Struct. 2021;241:112423.
[3] Ngo TT, Pham TM, Hao H, Chen W, Elchalakani M. Performance of monolithic and dry joints with GFRP bolts reinforced with different fibres and GFRP bars under impact loading. Eng Struct. 2021;240:112341.
[4] Li Z, Chen W, Hao H, Cui J, Shi Y. Experimental study of multi-layer folded truncated structures under dynamic crushing. Int J Impact Eng. 2019;131:111-22.
[5] Ha NS, Lu G, Xiang X. High energy absorption efficiency of thin-walled conical corrugation tubes mimicking coconut tree configuration. Int J Mech Sci. 2018;148:409-21.
[6] Ha NS, Lu G, Xiang X. Energy absorption of a bio-inspired honeycomb sandwich panel. J Mater Sci. 2019;54:6286-300.
[7] Le TV, Ghazlan A, Ngo T, Nguyen T, Remennikov A. A comprehensive review of selected biological armor systems – From structure-function to bio-mimetic techniques. Compos Struct. 2019;225:111172.
[8] Choudhary NS, Goel MD, Panchal S. Numerical Analysis of Innovative Sacrificial Protection System under Blast Loading. Practice Periodical on Structural Design and Construction. 2022;27:04021075.
[9] Van Paepegem W, Palanivelu S, Degrieck J, Vantomme J, Reymen B, Kakogiannis D et al. Blast performance of a sacrificial cladding with composite tubes for protection of civil engineering structures. Compos Part B: Eng. 2014;65:131-46.
[10] Ha NS, Pham TM, Chen W, Hao H, Lu G. Crashworthiness analysis of bio-inspired fractal tree-like multi-cell circular tubes under axial crushing. Thin-Walled Structures. 2021;169:108315.
[11] Tran P, Ghazlan A, Ngo TD. Chapter 8 - Design and Modeling of Bio-inspired Lightweight Composite Panels for Blast Resistance. In: Mouritz AP, Rajapakse YDS, editors. Explosion Blast Response of Composites: Woodhead Publishing; 2017. p. 201-31.

[12] Codina R, Ambrosini D, de Borbón F. New sacrificial cladding system for the reduction of blast damage in reinforced concrete structures. Int J Prot Struct. 2017;8:221-36.
[13] Hanssen AG, Enstock L, Langseth M. Close-range blast loading of aluminium foam panels. Int J Impact Eng. 2002;27:593-618.
[14] Ma GW, Ye ZQ. Energy absorption of double-layer foam cladding for blast alleviation. Int J Impact Eng. 2007;34:329-47.
[15] Hazizan MA, Cantwell WJ. The low velocity impact response of an aluminium honeycomb sandwich structure. Compos Part B: Eng. 2003;34:679-87.
[16] Queheillalt DT, Wadley HNG. Pyramidal lattice truss structures with hollow trusses. Materials Science and Engineering: A. 2005;397:132-7.
[17] Xiong J, Vaziri A, Ma L, Papadopoulos J, Wu L. Compression and impact testing of two-layer composite pyramidal-core sandwich panels. Compos Struct. 2012;94:793-801.
[18] Wicks N, Hutchinson JW. Performance of sandwich plates with truss cores. Mech Mater. 2004;36:739-51.
[19] Cao TNT, Luong VH, Vo HN, Nguyen XV, Bui VN, Tran MT et al. A Moving Element Method for the Dynamic Analysis of Composite Plate Resting on a Pasternak Foundation Subjected to a Moving Load. International Journal of Computational Methods. 2018;16:1850124.
[20] Yang G, Hou C, Zhao M, Mao W. Comparison of convective heat transfer for Kagome and tetrahedral truss-cored lattice sandwich panels. Sci Rep. 2019;9:3731.
[21] Le VT, Ha NS, Goo NS. Advanced sandwich structures for thermal protection systems in hypersonic vehicles: A review. Compos Part B: Eng. 2021;226:109301.
[22] Abdolrahim N, Liaghat G, Askari H. Experimental study of low velocity impact on Sandwich panels with honeycomb core and Comparison with the FEM results2013.
[23] Liu J, Chen T, Zhang Y, Wen G, Qing Q, Wang H et al. On sound insulation of pyramidal lattice sandwich structure. Compos Struct. 2019;208:385-94.
[24] Ehsan Moosavimehr S, Srikantha Phani A. Sound transmission loss characteristics of sandwich panels with a truss lattice core. The Journal of the Acoustical Society of America. 2017;141:2921-32.
[25] Ha NS, Lu G. Thin-walled corrugated structures: A review of crashworthiness designs and energy absorption characteristics. Thin-Walled Structures. 2020;157:106995.
[26] Ha NS, Lu G, Shu D, Yu TX. Mechanical properties and energy absorption characteristics of tropical fruit durian (Durio zibethinus). Journal of the Mechanical Behavior of Biomedical Materials. 2020;104:103603.
[27] Ha NS, Lu G. A review of recent research on bio-inspired structures and materials for energy absorption applications. Compos Part B: Eng. 2020;181:107496.
[28] Ha NS, Pham TM, Hao H, Lu G. Energy absorption characteristics of bio-inspired hierarchical multi-cell square tubes under axial crushing. Int J Mech Sci. 2021;201:106464.
[29] Vo NH, Pham TM, Bi K, Hao H. Model for analytical investigation on meta-lattice truss for low-frequency spatial wave manipulation. Wave Motion. 2021;103:102735.
[30] Liu Y, Shen X, Su X, Sun CT. Elastic Metamaterials With Low-Frequency Passbands Based on Lattice System With On-Site Potential. J Vib Acoust. 2016;138:021011--10.
[31] Vo NH, Pham TM, Bi K, Chen W, Hao H. Stress Wave Mitigation Properties of Dual-meta Panels against Blast Loads. Int J Impact Eng. 2021;154:103877.
[32] Xu C, Chen W, Hao H. The influence of design parameters of engineered aggregate in metaconcrete on bandgap region. J Mech Phys Solids. 2020;139:103929.
[33] Jin H, Hao H, Hao Y, Chen W. Predicting the response of locally resonant concrete structure under blast load. Constr Build Mater. 2020;252:118920.

[34] Xu C, Chen W, Hao H, Bi K, Pham TM. Experimental and numerical assessment of stress wave attenuation of metaconcrete rods subjected to impulsive loads. Int J Impact Eng. 2022;159:104052.
[35] Xu C, Chen W, Hao H, Jin H. Effect of engineered aggregate configuration and design on stress wave attenuation of metaconcrete rod structure. International Journal of Solids and Structures. 2021;232:111182.
[36] Xu C, Chen W, Hao H, Pham TM, Bi K. Damping properties and dynamic responses of metaconcrete beam structures subjected to transverse loading. Constr Build Mater. 2021;311:125273.
[37] Xiang X, Fu Z, Zhang S, Lu G, Ha NS, Liang Y et al. The mechanical characteristics of graded Miura-ori metamaterials. Mater Des. 2021;211:110173.
[38] Chen JS, Sharma B, Sun CT. Dynamic behaviour of sandwich structure containing spring-mass resonators. Compos Struct. 2011;93:2120-5.
[39] Sharma B, Sun CT. Impact load mitigation in sandwich beams using local resonators. J Sandw Struct Mater. 2015;18:50-64.
[40] La Salandra V, Wenzel M, Bursi OS, Carta G, Movchan AB. Conception of a 3D Metamaterial-Based Foundation for Static and Seismic Protection of Fuel Storage Tanks. 2017;4.
[41] Vo NH, Pham TM, Hao H, Bi K, Chen W, Ha NS. Blast resistant enhancement of meta-panels using multiple types of resonators. Int J Mech Sci. 2022;215:106965.
[42] Vo NH, Pham TM, Hao H, Bi K, Chen W. A reinvestigation of the spring-mass model for metamaterial bandgap prediction. Int J Mech Sci. 2022;221:107219.
[43] Hallquist JJLSTC. LS-Dyna Theory manual, March 2006. 2012.
[44] Flores-Johnson EA, Shen L, Guiamatsia I, Nguyen GD. Numerical investigation of the impact behaviour of bioinspired nacre-like aluminium composite plates. Compos Sci Technol. 2014;96:13-22.
[45] Tran P, Linforth S, Ngo TD, Lumantarna R, Nguyen TQ. Design analysis of hybrid composite anti-ram bollard subjected to impulsive loadings. Compos Struct. 2018;189:598-613.
[46] Ramezani M, Ripin ZM, Ahmad R. Plastic bulging of sheet metals at high strain rates. The International Journal of Advanced Manufacturing Technology. 2010;48:847-58.
[47] Alil L-C, Matache L-C, Sandu S. Numerical Simulation of a Ballistic Impact on Tensylon® UHMWPE Laminates Using the Plastic Kinematic Model in LS-Dyna®. Journal of Military Technology. 2018;1:43-50.
[48] Lee K. Effects on the various rubber fenders of a tripod offshore wind turbine substructure collision strength due to boat. Ocean Engineering. 2013;72:188-94.
[49] Chivapornthip P, Bohez ELJ. Dependence of bulk viscosity of polypropylene on strain, strain rate, and melt temperature. Polym Eng Sci. 2017;57:830+.
[50] Huang HH, Sun CT. Wave attenuation mechanism in an acoustic metamaterial with negative effective mass density. New J Phys. 2009;11:013003.
[51] Aryal B, Morozov EV, Wang H, Shankar K, Hazell PJ, Escobedo-Diaz JP. Effects of impact energy, velocity, and impactor mass on the damage induced in composite laminates and sandwich panels. Compos Struct. 2019;226:111284.
[52] Liu J, Chen W, Hao H, Wang Z. Numerical study of low-speed impact response of sandwich panel with tube filled honeycomb core. Compos Struct. 2019;220:736-48.
[53] Chai GB, Zhu S. A review of low-velocity impact on sandwich structures. Proceedings of the Institution of Mechanical Engineers, Part L: Journal of Materials: Design and Applications. 2011;225:207-30.

List of Figures

Fig. 22. Impact loading with various velocities, (a) time-histories, and (b) FFT.

Fig. 23. Undeformed and deformed contour of the meta-panel under impact with various velocities.

Fig. 24. Schematic diagrams of models to calculate (a) k_2 and (b) k_1.

List of Tables

Appendix

With an attempt to estimate the accurate values of the spring stiffness k_i (i=1,2), the FE model was built. A constant force F which is depicted in Fig. 24 (a) is applied to the model to calculate the value of shear spring stiffness k_2 between the core and the outer tube while two constant force F are put in two directions of the model to estimate the values of k_1 shown in Fig. 24(b). As seen in Fig. 24 (a) and 24 (b), the average displacements monitored at the surfaces are denoted as u_i (i=1,2,3) and captured by commercial software. The boundary condition for all edges of the outer shell is clamped. The relation between stiffness and displacement of the unit model which is shown in will be achieved as following [31]:

$$\begin{aligned} k_1(u_1+u_2)+k_2u_1 &= F \\ k_2u_3 &= F \end{aligned} \tag{17}$$

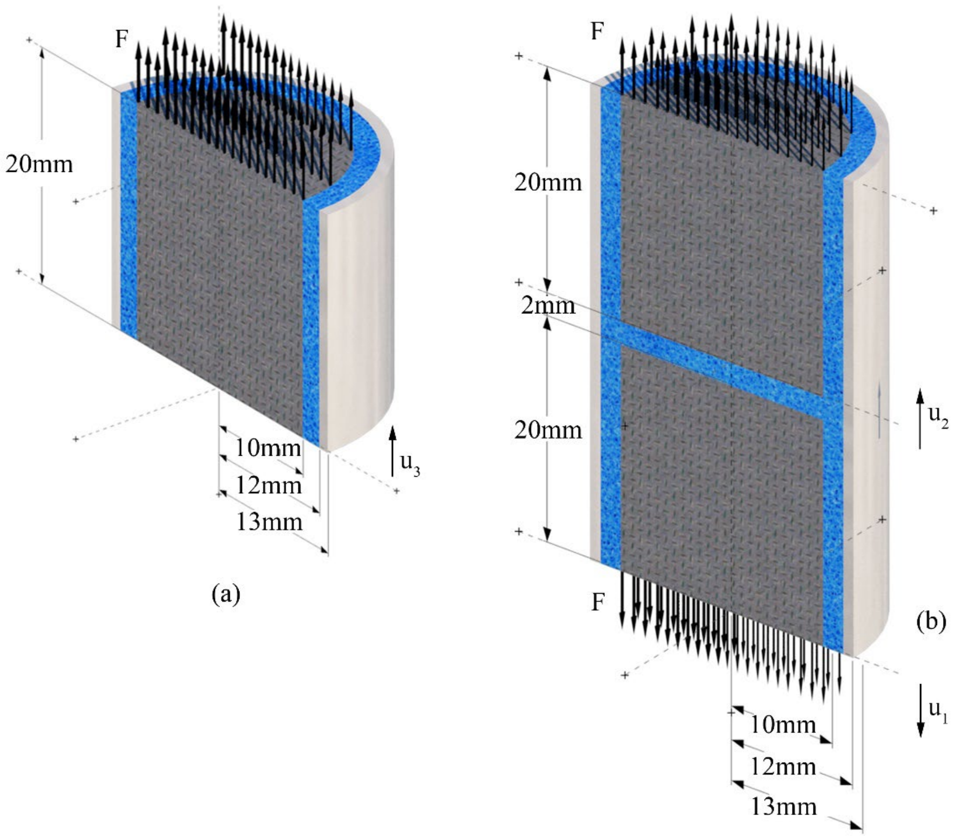

Fig. 24. Schematic diagrams of models to calculate (a) k_2 and (b) k_1.